ESD-TR-75-253

12

See 147

ADA020339

1

Optics Research

1975

Prepared for the Advanced Research Projects Agency
under Electronic Systems Division Contract F19628-73-C-0002 by

Lincoln Laboratory

MASSACHUSETTS INSTITUTE OF TECHNOLOGY

LEXINGTON, MASSACHUSETTS

Approved for public release; distribution unlimited.

DDC
RECEIVED
FEB 10 1976
D

The work reported in this document was performed at Lincoln Laboratory, a center for research operated by Massachusetts Institute of Technology. This work was sponsored in part by the Advanced Research Projects Agency of the Department of Defense (ARPA Order 600) under Contract F19628-73-C-0002. Where noted, research sponsored by the Environmental Protection Agency and National Science Foundation is included.

This report may be reproduced to satisfy needs of U.S. Government agencies.

The views and conclusions contained in this document are those of the contractor and should not be interpreted as necessarily representing the official policies, either expressed or implied, of the Defense Advanced Research Projects Agency of the United States Government.

This technical report has been reviewed and is approved for publication.

FOR THE COMMANDER

Eugene C. Raabe, Lt. Col., USAF
Chief, ESD Lincoln Laboratory Project Office

Non-Lincoln Recipients

PLEASE DO NOT RETURN

Permission is given to destroy this document when it is no longer needed.

ACCESSION for
NTIS White Section
DDC Buff Section
UNANNOUNCED
JUSTIFICATION
BY
DISTRIBUTION AVAILABILITY CODES
Dist. AVAIL. and or SPECIAL
A

MASSACHUSETTS INSTITUTE OF TECHNOLOGY

LINCOLN LABORATORY

OPTICS RESEARCH

SEMIANNUAL TECHNICAL SUMMARY REPORT
TO THE
ADVANCED RESEARCH PROJECTS AGENCY

1 JANUARY – 30 JUNE 1975

ISSUED 7 NOVEMBER 1975

DDC
RECEIVED
FEB 10 1976
D

Approved for public release; distribution unlimited.

LEXINGTON MASSACHUSETTS

ABSTRACT

This report covers work of the Optics Division at Lincoln Laboratory for the period 1 January through 30 June 1975. The topics covered are laser technology and propagation and pollution studies.

Additional information on the optics program may be found in the ARPA/STO Program Semiannual Technical Summary Reports to the Advanced Research Projects Agency.

PAGE BLANK-NOT FILMED

CONTENTS

Abstract		iii
Introduction		vii
Reports on Optics Research		viii
Organization		x
I.	LASER TECHNOLOGY AND PROPAGATION	1
A.	Propagation	1
1.	Laboratory Experiment on Thermal Blooming	1
2.	Multiple-Pulse Blooming: Comparison of Experiment with Theory	9
3.	Fog Blooming Measurements	17
B.	Laser Effects	20
1.	Large-Spot Thermal Coupling Measurements	20
2.	Microwave Measurements of a Laser-Generated Surface Plasma	25
C.	Long-Term Frequency Stabilization of CO_2 Lasers	29
II.	POLLUTION STUDIES	37
A.	Participation in the St. Louis Regional Air Pollution Study (RAPS) of the U.S. Environmental Protection Agency	37
1.	Introduction	37
2.	RAPS Measurements - Summary	37
3.	RAPS Measurements - Data	37
4.	Future Plans	41
B.	Long-Path Ambient Monitoring of Nitric Oxide	43

PRECEDING PAGE BLANK-NOT FILMED

INTRODUCTION

I. LASER TECHNOLOGY AND PROPAGATION

A laboratory experiment has been performed which compensates for thermal blooming by means of an adaptive mirror. The mirror added predictive phase corrections according to the Bradley-Herrmann calculations, and significant increases in intensity were produced.

A multiple-pulse propagation measurement program that demonstrates good agreement between the experimental data and the predictions of the Bradley and Herrmann steady state blooming model has been completed.

Preliminary experimental results are reported for second-pulse blooming of high-energy CO_2 laser pulse propagating through a laboratory fog environment. The fog densities ranged from 2 to 8 gm/m^3, and the propagation path length was 5 meters. Negligible first-pulse blooming was observed. The second-pulse blooming tended to decrease with increasing fog density. The analysis of the data is continuing.

Thermal coupling of pulsed radiation to aluminum and titanium targets was measured for spot areas $\geq 6.3\ cm^2$. These measurements showed that (1) for low fluences, enhanced coupling is retained for large spots with most of the energy absorbed within the irradiated spot, (2) above the target dependent threshold, the thermal coupling is material independent, and (3) more energy can be delivered to a target at reduced ambient pressure than at atmospheric pressure.

Preliminary measurements have been made on microwave transmission, reflection, and in-band radiation for a laser-generated surface plasma. The initial experiments indicate that the reflection and transmission of microwaves is consistent with theory.

Significant improvements have been obtained in the long-term frequency stabilization of CO_2 lasers by means of the 4.3-μm $(00^01) \rightarrow (00^00)$ fluorescence technique. A hundred-fold increase in signal-to-noise ratios at 4.3 μm has been achieved. The lasers remained firmly locked to the CO_2 line center with as little as ±2 kHz frequency dither.

II. POLLUTION STUDIES

Successful field monitoring of ambient carbon monoxide levels over long paths in the St. Louis area was performed during August to October 1974. The CO measurements with the tunable diode laser system inside a mobile van were a part of the Regional Air Pollution Study sponsored by the U.S. Environmental Protection Agency. Recently, the monitoring capabilities have been extended to include nitric oxide, NO. Field experiments performed in Cambridge, Massachusetts, measured large amounts of NO in the exhaust of commercial trucks and buses.*

* This paragraph describes the work performed at Lincoln Laboratory under the sponsorship of the National Science Foundation (Research Applied to National Needs), with partial support from the U.S. Environmental Protection Agency.

REPORTS ON OPTICS RESEARCH

1 January through 30 June 1975

PUBLISHED REPORTS

Journal Articles

JA No.			
4359	Two-Dimensional Nonrecursive Filters	J. G. Fiasconaro	Chapter in Digital Picture Processing, T. S. Huang, Editor (Springer-Verlag, Berlin, 1975)
4398	Long-Path Monitoring of Atmospheric Carbon Monoxide by a Tunable Laser System	R. T. Ku E. D. Hinkley J. O. Sample	Appl. Opt. 14, No. 4, 854 (April 1975)
4421	Nonchemical HF Pulse Laser Pumped by e-Beam-Sustained Discharge	R. M. Osgood, Jr. D. L. Mooney	Appl. Phys. Lett. 26, No. 4, 201 (15 February 1975), DDC AD-A008305/5
4435	Impulsive Loading of Targets by HF Laser Pulses	S. Marcus J. E. Lowder	J. Appl. Phys. 46, No. 5, 2293 (May 1975)
4477	10.6-μm FM-Chirp Radar Using Narrow-Band Correlation Detection	W. E. Bicknell L. R. Tomasetta R. H. Kingston	IEEE J. Quantum Electron. QE-11, No. 6, 308 (June 1975)

* * * * *

UNPUBLISHED REPORTS

Meeting Speeches*

MS No.			
3940	Long-Path Laser Monitoring of CO in the St. Louis Area	L. W. Chaney† W. A. McClenny† R. T. Ku	Air Pollution Control Association, Boston, Massachusetts, 15-20 June 1975
3944	Tunable Infrared Laser Studies of the Polluted Atmosphere	R. T. Ku E. D. Hinkley	Optical Society of America, Anaheim, California, 19-21 March 1975
3944A	Long-Path Laser Monitoring of Atmospheric Pollutants	E. D. Hinkley	Seminar, Environmental Protection Agency, Las Vegas, Nevada, 1 May 1975

* Titles of Meeting Speeches are listed for information only. No copies are available for distribution.

† Author not at Lincoln Laboratory.

MS No.			
3956	Laser Heating of Metallic Surfaces	S. Marcus J. E. Lowder S. K. Manlief D. L. Mooney	1975 IEEE/OSA Conference on Laser Engineering and Applications, Washington, D. C., 28-30 May 1975
4023	Frequency Stabilization of CO_2 Lasers	C. Freed	Twenty-Ninth Annual Frequency Control Symposium, Atlantic City, 28-30 May 1975
4024	Infrared Chirp Radar with 30 cm Range Resolution	R. H. Kingston	Electrical Engineering Department Seminar at M.I.T., 20 March 1975
4053	Laser Monitoring of the Atmosphere	E. D. Hinkley	(Invited paper) Los Alamos Scientific Laboratory, Los Alamos, New Mexico, 29 April 1975
4072	Laser Spectroscopic Instrumentation and Techniques	E. D. Hinkley	Expert Conference on Laser Spectroscopy of the Atmosphere, Rjukan, Norway, 18 June 1975

ORGANIZATION

OPTICS DIVISION

R. H. Rediker, *Head*
L. B. Anderson, *Associate Head*
W. J. Hudson, *Assistant*
V. H. Rees, *Staff*

ADVANCED TECHNIQUES AND SYSTEMS

S. Edelberg, *Leader*
J. F. Crowder, *Assistant Leader*

Bonanno, J. F.
Burlingame, J. G.
Bloser, J. J.
Bradley, J. C.
Buschner, J. D.
Decker, D. D.
Ellis, R. H.
Ferdinand, A. P., Jr.
Hanshaw, P. D.
Hopkins, J. D.
Kenyon, R. L.
Ku, R. T.
Lowrimore, D. F.
Lowrie, J. S.
Mosakowski, S. K.
Morrison, S.
McSheehy, R. H.
Neil, T. P.
O'Neil, R. A.
Pettingill, J. C.
Quist, T. M.
Semmler, J. O.
Sullivan, F. M.
Thomas, M. A.
Zwicker, H. R.

OPTO-RADAR SYSTEMS

A. B. Gschwendtner, *Leader*
H. Kleiman, *Assistant Leader*

Beckmann, W. J.
Billups, R. B.
Cordova, R. J.
DiMarzio, F. B.
Edwards, D. M.
Hull, R. J.
Johns, T. W., II
Kercher, A.
Lammer, D. F.
Martin, J. S.
McPhee, J. M.
Merrill, J. R.
Parenti, R. R.
Tomczak, S. P.
Tyson, J. D.
Zieman, H. E.

INFRARED RADAR

R. H. Kingston, *Leader*
P. A. Ingwersen, *Associate Leader*
L. J. Sullivan, *Associate Leader*
J. Z. Holtz, *Assistant Leader*

Bates, D. H.
Bicknell, W. E.
Capes, R. N., Jr.
Daley, J. A., Jr.
Franciomore, J. G.
Freed, C.
Fulton, M. J.
Malling, L. R.
Marapodi, J. V.
O'Donnell, R. G.
Osgood, R. M., Jr.
Parker, A. C.
Scouler, W. J.
Sweezey, L. W.
Teoste, R.
Tomasetta, L. R.
Valcourt, G. L., Jr.
Ziegler, R. L.
Zimmerman, M. D.

APPLIED RADIATION

L. C. Marquet, *Leader*
E. S. Cotton, *Assistant Leader*
D. A. Page, *Assistant Leader*

Ariel, F. D.
Bollman, R. A.
Braman, C. E.
Brennan, M. J.
Chaulk, L. W.
Corbostero, D. M.
Finne, P. C.
Fouche, D. G.
Grant, P. L.
Herrmann, J.
Huber, E. J.
Johnson, F. B.
Johnson, J. Q.
Johnson, R. E.
Kafalas, P.
Kelsall, D.
Kileline, C. W.
Knowlton, R. C.
Kocher, D. G.
Kramer, R.
Lifsitz, J. R.
Marshall, A. P.
McPherson, R. D.
Murency, A. J.
Mudgett, D. A.
Perry, F. H.
Pike, R. A.
Pirroni, J. S.
Pitts, R. F.
Prade, G. C.
Primmerman, C. A.
Shey, S. Y.
Stiehl, W. A.
Swedberg, J. L.
Theriault, J. R.
Vernon, H. M.
Weaver, L. D.

I. LASER TECHNOLOGY AND PROPAGATION

A. PROPAGATION

1. Laboratory Experiment on Thermal Blooming

As a laser beam passes through an absorbing medium, it heats the medium causing the index of refraction along its path to change. The changing index of refraction, in turn, causes the beam to be spread or bloomed. It has been proposed that one can compensate for this thermal blooming by using an adaptive-optics system to add appropriate phase corrections at the beam transmitter. We have in progress a laboratory experiment designed to test the efficacy of using this technique to compensate for thermal blooming.

a. Deformable-Mirror System

We are applying phase corrections to the beam by means of a deformable-mirror system. The deformable mirror consists of a monolithic disc of piezoelectric crystal into which is placed an array of 57 independently actuated electrodes. These electrodes can produce surface deformations of ±0.5 μm over an active area 1.5 inches in diameter. The mirror surface is a metalized glass disc cemented on the piezoelectric crystal.

For the preliminary experiments with this mirror, the relative voltages of the 57 actuators have been set to give the relative phase profile shown in Fig. I-1. This profile has been calculated by Bradley and Hermann[1] to give the maximum correction for a truncated Gaussian beam undergoing forced-convection-dominated thermal blooming. In the experiments reported here, we manually varied the overall amplitude but did not vary the shape of the deformation. In later experiments, we plan to vary the shape of the profile and also to dither the amplitude.

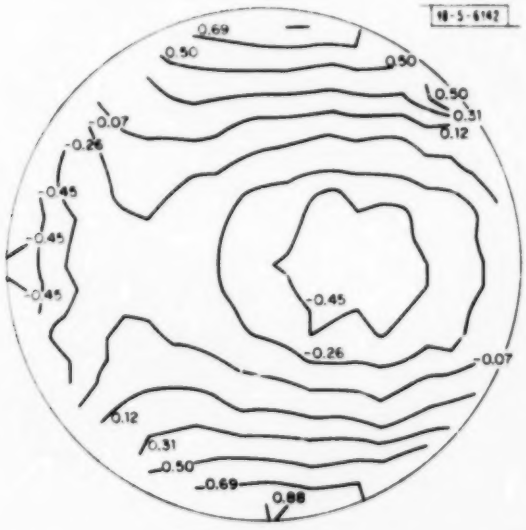

Fig. I-1. Surface contour on the deformable mirror. This profile was determined from computational analysis of the laser-beam propagation. Contours are labeled in units of wavelength.

b. Experimental Conditions

The experimental arrangement is shown in Fig. I-2. With the exception of the deformable mirror the setup is similar to that used in earlier thermal-blooming experiments.[2,3,4] We use an argon laser that produces a Gaussian beam with up to 2 watts of useful power at 5145 Å. The beam is expanded to make the $1/e^2$ diameter 1.5 inches, is truncated at this diameter, and is reflected from the deformable mirror. The beam is then contracted and is slewed through the absorbing cell by a variable-speed slewing mirror. In the focal plane just beyond the cell, we have a row of 50-μm pinholes at a slight angle to the slewed beam. By detecting the light coming through these pinholes, we are able to measure both the intensity and the shape of the bloomed beam. Additionally, we have the capability to photograph the beam as it leaves the gas cell.

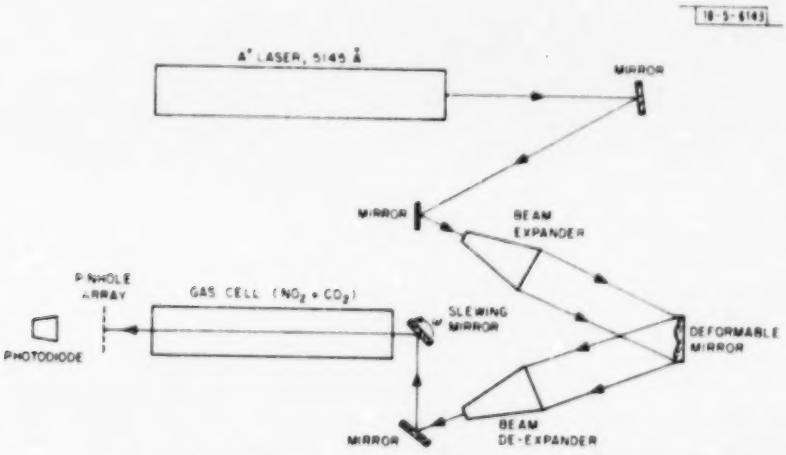

Fig. I-2. Schematic of the experimental arrangement.

The gas cell is filled with a few Torr of NO_2, enough to absorb ~50 percent of the incident radiation in the 1.5-m-long tank. Since we are interested in studying the thermal blooming of a slewed beam (that is, one in which forced convection is the dominant cooling mechanism), the gas cell is mounted vertically to minimize free-convection cooling, and one atmosphere of CO_2 is added to the cell to reduce conduction cooling. Mounting the gas cell vertically effectively eliminates free-convection effects; but, unfortunately, conduction effects are not always negligible and must be taken into account.

As shown by Bradley and Hermann, the propagation of a slewed beam through an absorbing medium can be characterized by the four dimensionless numbers:

$$\text{Absorption Number} - N_A \equiv \alpha R$$

$$\text{Fresnel Number} - N_F \equiv ka^2/R$$

$$\text{Slewing Number} - N_\omega \equiv \omega R/v$$

$$\text{Distortion Number} - N_D \equiv (1/\rho c_p \epsilon_o)(\partial\epsilon/\partial T)(\alpha PkR/av)$$

where α is the absorption coefficient, R is the range, k is the wave number, a is the 1/e radius at the cell entrance, ω is the slewing frequency, v is the constant crosswind velocity,

P is the incident power, and $(1/\rho c_p \epsilon_o)(\partial\epsilon/\partial T)$ characterizes the change in index of refraction of the heated gas. For our laboratory experiment an additional dimensionless number is required:

$$\text{Conduction Number} - N_C \equiv \kappa/\sqrt{2}\, av$$

where κ is the thermal diffusivity.

The actual experimental conditions are given by the following set of parameters:

$\alpha = 4.6 \times 10^{-3}$ cm^{-1}

R = 150 cm

$k = 1.22 \times 10^{5}$ cm^{-1}

a = 0.25 cm

ω = 0 to 0.2 rad/sec (variable)

v = 0 to 3 cm/sec (variable)

p = 0.03 to 1 watt (variable)

$(1/\rho c_p \epsilon_o)(\partial\epsilon/\partial T) = 1.95 \times 10^{-3}$ J^{-1} cm^3

$\kappa = 0.11$ cm^2-sec^{-1}

$N_A = 0.69$

$N_F = 45$

N_ω = 7.5 to 30 (variable)

$N_D = 686\ P/v$ (variable)

N_C = 0.1 to ∞ (variable)

The three basic variables in these experiments were the input power at the cell entrance, P, the slew velocity, ω, and the constant crosswind velocity, v, which could be varied independently of ω by changing the distance from the slewing mirror to the cell entrance. These variables enabled us to test the dependence of the thermal blooming on the dimensionless numbers N_ω, N_D, and N_C. We can also vary N_A and N_F, but in these experiments no attempt was made to systematically study the effect of these parameters on the thermal blooming.

c. Experimental Results

(1) Results of Varying Power

In Fig. I-3 we show the peak focal-plane intensity plotted against input power for the uncorrected beam, the corrected beam, and the hypothetical situation of absorption with no blooming. Varying the power is equivalent to varying N_D, since $N_D \propto P$. The uncorrected curve was taken with the deformable mirror in the flat condition; the corrected curve was obtained by adjusting the amplitude of the mirror deformation to get the maximum possible intensity at each power.

The uncorrected curve exhibits the classic thermal-blooming behavior: the intensity first increases with increasing power and then, after a certain critical power, P_c, begins to decrease rapidly with increasing power. Note, however, that at a power $P \approx 2P_c$ there is an inflection point in the curve, after which the intensity decreases much more slowly with increasing power.

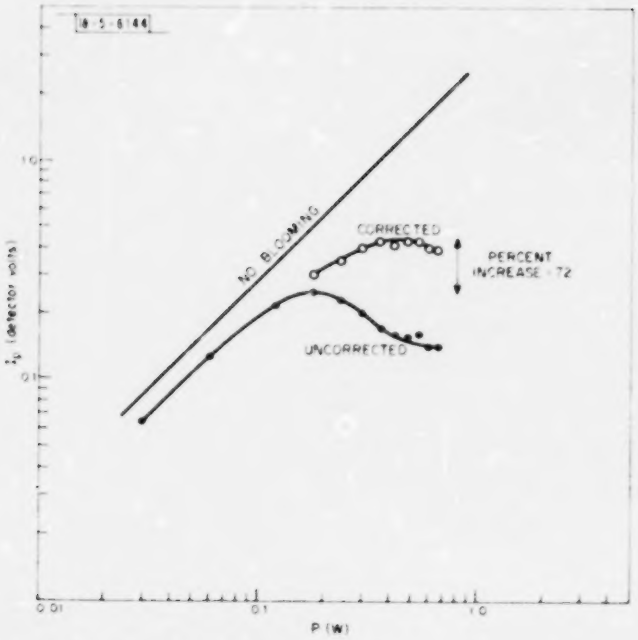

Fig. I-3. Focal-plane intensity vs input power for corrected and uncorrected curves. The straight line would be the intensity if there were absorption but no blooming. v = 1.65 cm/sec, N_C = 0.19, N_ω = 10. Other parameters are described in text.

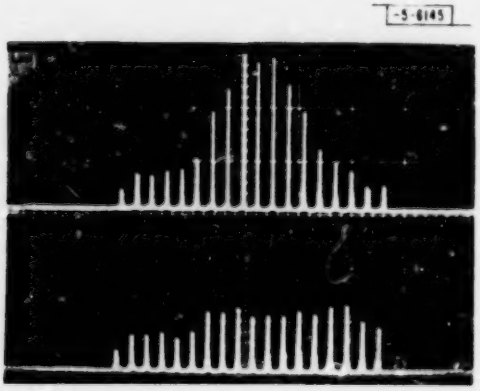

Fig. I-4. Intensity through pinhole array for severely bloomed conditions at P = 0.45 watt. Lower curve: uncorrected. Upper curve: corrected. The pinholes are 0.002 in. diameter and 0.096 in. apart. Parameters as in Fig. I-7.

This behavior indicates that the intensity loss may be less than anticipated in the severely bloomed regime beyond P_c.

As expected, the corrected curve shifts upward to higher intensities and outward to a higher critical power. We observe that the peak intensity increases 72 percent over the uncorrected case and that at certain powers there is a factor of 3 increase in intensity. This result is representative: we have consistently achieved improvements in peak intensity of ~70 percent. These improvements are in reasonable agreement with those predicted by our computer code.

Figure I-4 shows oscilloscope traces of the detector voltage as the beam sweeps across our detector array. The bottom trace shows the severely bloomed beam at P = 0.45 watt; the upper trace shows the corrected beam at the same power. We see that the peak intensity has increased by almost a factor of 3 and that the beam shape has been greatly improved.

Figure I-5 shows actual photographs of the beam in the focal plane. In the top picture we see the characteristic crescent-shaped bloomed beam. In the next picture we see the corrected beam, reduced in size and with only a slight remaining indication of a crescent shape. For comparison, the bottom photograph shows the low-power, unbloomed beam. (The somewhat elliptical shape results from the fact that the shutter speed is not fast enough to freeze the beam.) Note that both the corrected and uncorrected bloomed beams are shifted into the wind relative to the unbloomed beam. We observe that, consistent with the intensities shown in Fig. I-3, the corrected spot size is still larger than the unbloomed spot size.

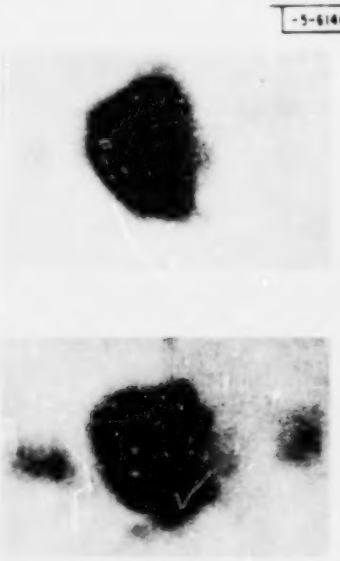

Fig. I-5. Actual photographs of the bloomed, corrected, and unbloomed beam. The top two pictures correspond to the pinhole traces of Fig. I-4. The slight ellipticity results from insufficient shutter speed.

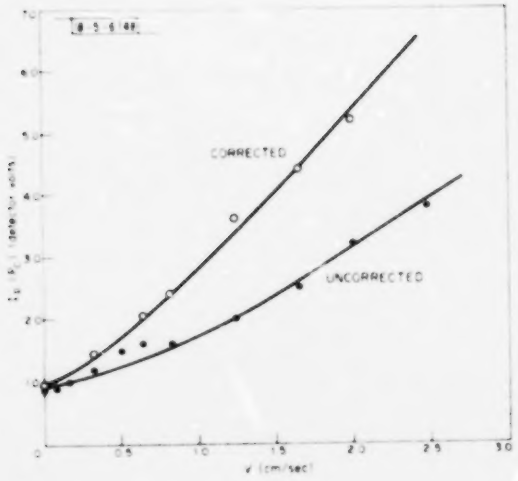

Fig. I-6. Critical power vs constant crosswind velocity for corrected and uncorrected cases. N_ω = 10. Other conditions as listed above.

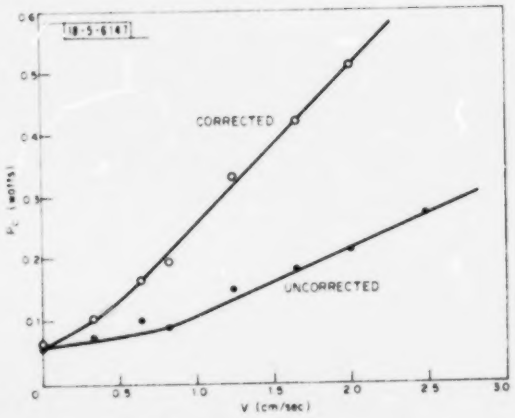

Fig. I-7. Intensity at the critial power vs constant crosswind velocity for corrected and uncorrected cases. N_ω = 10. Other conditions as listed above.

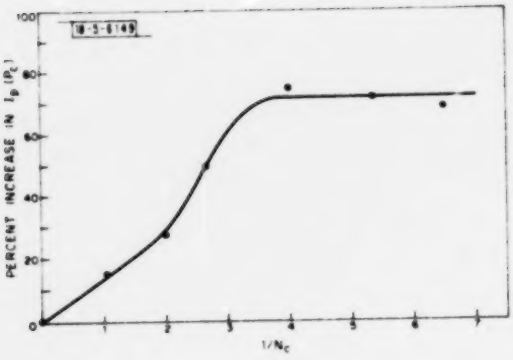

Fig. I-8. Percentage increase in maximum intensity vs $1/N_C$. Data taken from Fig. I-12.

(2) Results of Varying Slew Frequency

In Figs. I-6, I-7, and I-8, we show the results of varying the slew frequency, ω. Because of the experimental arrangement, this variation changes the effective crosswind velocity, v, while keeping N_ω constant. Changing v changes both N_D and N_C, since these dimensionless numbers are both proportional to $1/v$.

Figure I-6 shows the critical power, P_c, plotted against v. Since $N_D \propto P/v$, P_c should be proportional to v if all other dimensionless numbers are unchanged. We see that above $v \approx 1$ cm/sec P_c is, in fact, proportional to v for both the corrected and uncorrected curves. Below $v \approx 1$ cm/sec, however, both curves deviate from this behavior, flattening out to reach $P_c = 0.2$ watt for $v = 0$. Figure I-7 shows the peak intensity plotted against v for corrected and uncorrected cases. These curves show the same basic behavior as those of Fig. I-6: again for $v > 1$ cm/sec the curves are linear, but for $v < 1$ cm/sec the curves deviate and eventually reach a common, non-zero peak intensity at $v = 0$.

The behavior shown in Figs. I-6 and I-7 is readily explained by taking into account the variation of the conduction number with v. Above $v \approx 1$ cm/sec N_C is small, and the effect of conduction is negligible; thus, the cooling is dominated by forced convection, and P_c and the peak intensity are, as predicted, proportional to v. Below $v \approx 1$ cm/sec, however, conduction becomes important, resulting in higher critical powers and peak intensities than predicted without conduction. Eventually, as $v \rightarrow 0$ conduction dominates forced convection, and the peak intensity and critical power approach values determined by conduction alone. At $v = 1$ cm the conduction number is $N_C = 0.3$; thus, it appears from these results that if $N_C < 0.3$ conduction can be ignored compared to forced convection.

We see from Figs. I-6 and I-7 that as v decreases and conduction becomes more important, the deformable mirror becomes less effective at correcting for the thermal blooming. This result is better illustrated in Fig. I-8, where we plot the percentage increase in peak intensity against $1/N_C$. We observe that at $1/N_C = 0$, where conduction dominates, no improvement is obtained. As $1/N_C$ increases, the improvement first increases sharply and then, as conduction becomes negligible, levels off at the maximum value of ~70 percent. This behavior is precisely what was expected. The phase profile on our mirror was derived using a theoretical treatment that neglects conduction; thus, our correction should be most effective when conduction is negligible and should decrease in effectiveness as conduction becomes important.

(3) Results of Varying Slewing Number

By simultaneously changing the distance from the slewing mirror to the cell entrance and adjusting ω, we are able to change N_ω while keeping v constant. Increasing N_ω increases the cooling at the far end of the cell relative to that at the cell entrance; thus, as N_ω increases, the region over which significant blooming occurs is compressed towards the cell entrance. This compression of the blooming zone should make it easier for adaptive-optics systems to correct for the blooming.

Figure I-9 shows the peak intensity plotted against N_ω for both uncorrected and corrected cases. We observe that the uncorrected curve is nearly linear but that the corrected curve bends upwards as N_ω increases. In Fig. I-10, we plot the percentage increase in the peak intensity against N_ω. We observe that, as predicted, the phase correction is more effective at higher slewing numbers. At first the percentage improvement increases roughly linearly with

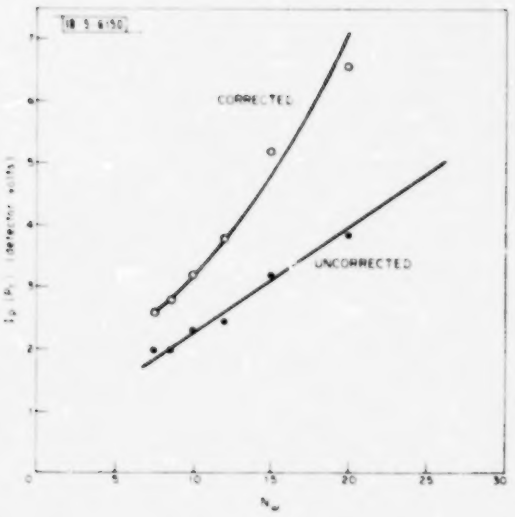

Fig. I-9. Intensity at the critical power vs slewing number. v = 1.65 cm/sec, N_C = 0.19. Other parameters as listed above.

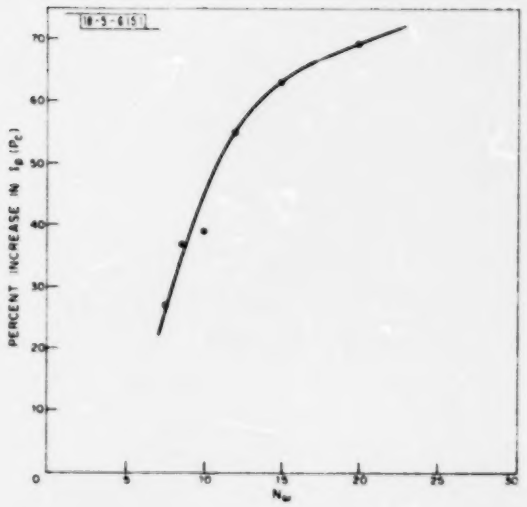

Fig. I-10. Percentage increase in maximum intensity vs slewing number. Data taken from Fig. I-13.

N_ω, but as N_ω is further increased the incremental improvement becomes smaller. Thus, there is some indication that a practical limit may be reached beyond which further reducing the blooming zone does not significantly improve the correction.

d. Conclusion

In this investigation, we have obtained the first experimental evidence of the feasibility of compensating for convection-dominated thermal blooming by using a deformable mirror to add phase corrections to the laser beam. We have conclusively demonstrated that this technique can produce significant increases in transmitted intensity. Further work is necessary to determine the limits of the correction method, but the basic applicability of the method has now been experimentally proven.

D. G. Fouche
C. A. Primmerman

2. Multiple-Pulse Blooming: Comparison of Experiment with Theory

In the preceding Optics Research Report (1974:2), we described the operational details of a laboratory-scale multiple-pulse thermal-blooming experiment using uniform crosswind and a 4.6-m absorption cell. In this report, we present the results of this completed measurement program. In the one-month effort, nearly 175 experiments were performed ($>10^4$ individual measurements); approximately half of these were found to be useful for testing the validity of the computer code. In general, the data are in excellent agreement with the predictions of the Bradley and Herrmann model for steady-state multiple-pulse blooming.

As we indicated previously, the experimental program was designed to test the limits and capabilities of this code. For a specific propagation condition, the inputs to the code are the (constant) energy per pulse (E_p), wind velocity (v_x), absorption coefficient (α), laser repetition frequency ($\nu = 1/\tau_p$), the laser energy distribution at the entrance to the absorption cell [$E(x, y, 0)$] and in the unbloomed focal plane $[E(x, y, R)]_{\alpha=0}$. The beam truncation (D_x, D_y) referenced to the cell entrance must also be uniquely specified. To satisfy the requirement of "no single-pulse blooming" implicit in the steady-state model, choices of these parameters are restricted to the a priori calculated parameter space illustrated in Fig. I-3 of Optics Research Report 1974:2.

Reasonably strong prerequisites on laser performance were required to perform a meaningful experiment. In Table I-1 the permissible limits in the experimental design are listed along with the measured laser output characteristics achievable during most of the experimental program. (A one-week measurements program preceding the propagation experiments allowed us to determine for the first time the multiple-pulse characteristics of this laser.)

For the energy and phase of the laser output, we normally used a circular or rectangular Gaussian-distributed uniphase beam with a specified truncation as the best approximation to the experimental conditions. This assumption was based on the results of mapping the energy distribution at the entrance to the absorption cell (the reference plane for overlap in a focused beam) and fitting a Gaussian beam to this distribution. The details of the aperture measurements are illustrated in Fig. I-11, where we plot the averaged energy distribution obtained by spatially scanning the laser beam at the entrance to the absorption cell; data were obtained with a 64-element calorimeter array described previously. On a scale of 1 mm per element in the scan direction and using both 3- and 15-mm slit aperture heights, energy distributions in the x- and the y-directions were found to be quite similar and both reasonably smooth. The entire aperture distribution was mapped by positioning the array through translation and rotation;

TABLE I-1

AERL LASER CHARACTERISTICS

Parameter	Experimental Design Parameters	Measured Parameters
1. Energy/Pulse, E_p	$\geq$10 J	$\leq$7 J
2. Pulse-to-Pulse Energy Variation, ΔE_p	$\leq$ ±10 percent	~ ±10 percent
3. Laser Repetition Rate, γ	10 – 100 Hz	1 – >200 Hz
Variation in γ	<2 percent	~2 percent
4. Pulse Length, t_p	5 μsec	~6 μsec
5. Beam Quality, β	$\leq$2	$\leq$1.2
6. Pulse-to-Pulse Variation in p, $\Delta\beta$	$\leq$15 percent	$\leq$10 percent
7. Aperture	2 × 4 cm (off-axis resonator)	a. $1.36 \times 3.03_{cm}$ (60 percent) b. $1.65 \times 3.4_{cm}$ (80 percent)
8. Pointing Stability		
(1) Translation	$\leq$ ±2 mm	$\leq$ ±3 mm
(2) Angular	$\leq$ ±150 μrad	~150 μrad

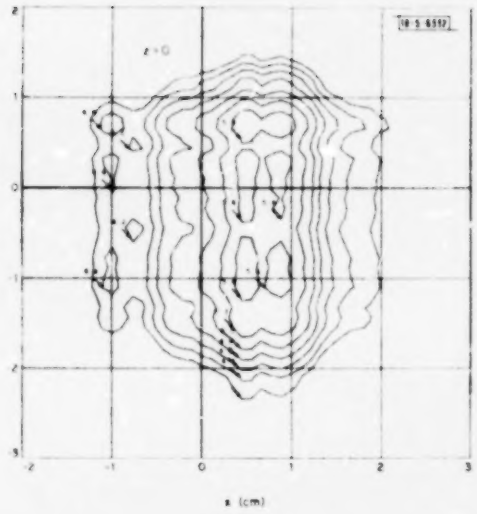

Fig. I-11. Averaged two-dimensional energy contour plot of AERL laser beam at the entrance to the absorption cell. Contours are separated by 2 dB.

typically 2 runs of 8 to 10 pulses were recorded at each position. Pulse to pulse and run to run, the measurements were reproducible and yielded the same qualitative picture as did a series of burn patterns. An x, y, energy matrix was generated from the averaged profile and was used as the source of amplitude input to the computer code. Phase information was approximated by propagating a unit amplitude plane wave from the laser cavity to the absorption cell entrance.

Some assymmetry in the plot in Fig. I-11 is due to a second angular mode present in this laser; this mode contains about 5 percent of the total energy. The experiment was arranged to keep this lobe downstream of the overlap region so that it did not influence the measurement; in the measurement plane, this mode focused ~3 cm from the primary beam.

The constructed-aperture distribution was used to calculate cases for several experimental conditions and found to give good agreement. When a two-dimensional Gaussian was fitted to the measured distribution at the half-energy points and assigned a truncation width, D_x from the measured zeros of the unbloomed far-field diffraction burn patterns, the predicted results did not differ significantly from those of the full x-y matrix predictions. Since the relative computer run costs of the two procedures differed by more than a factor of 10, the less expensive Gaussian approximation was used for theory comparisons, as described above.

In Fig. I-12(a) the measured E(x) distribution is plotted for the analytic (Gaussian) approximation. (The small hump on the left-hand side of the measured distribution is the aforementioned angular mode. The primary beam is approximately symmetric with the right-hand side of the distribution.) When the analytic approximation is propagated to the focal plane, the distribution in Fig. I-12(b) (solid line) is obtained. The dotted distribution is an experimental array measurement, peak normalized to unity. In the absence of the low-level background spray present in the real beam, the two distributions are nearly identical. Absolute accuracy of the array measurement is ±8.7 percent, or comparable to the plotted difference.

In a typical series of experiments, the parameters α, E_p, R, D_x, and ν are maintained constant. Overlap conditions are varied by changing wind velocity to generate a number of predetermined overlap numbers.

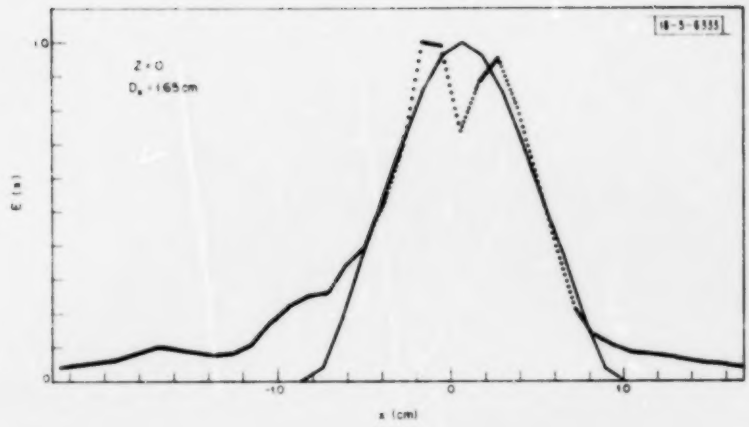

(a)

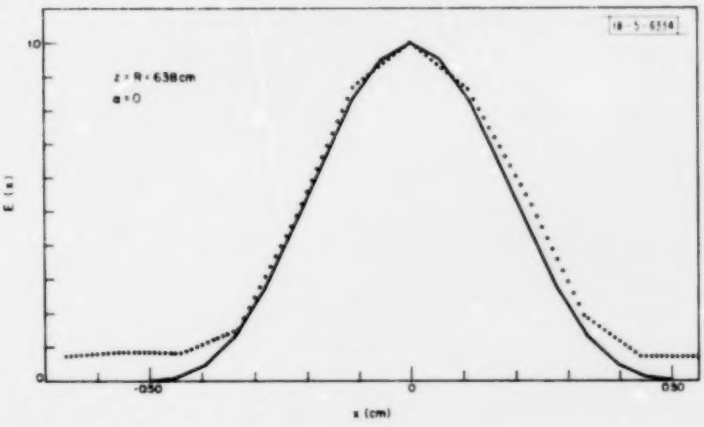

(b)

Fig. I-12. (a) One-dimensional energy distribution at the entrance to the absorption cell entrance (dotted line). The solid-line distribution is a truncated Gaussian distribution used to approximate the measured distribution in computer calculations. The lump on the left-hand side is a second low-energy mode that is separating angularly from the main beam. (b) Calculated one-dimensional energy distribution at focus, using the Gaussian approximation in Fig. I-12(a) (solid line). The dotted distribution is that measured with the array.

To insure that all experimental conditions appropriate for a valid comparison with theory were correct, the laser parameters as well as all influential parameters external to the laser (e.g., wind velocity, alignment, background vibration, etc.) were measured for each pulse in every experimental run of 8 to 15 pulses. Real-time data examination made it possible to detect deviations from acceptable conditions and to determine when steady state had been achieved; typically this occurred two to three pulses after the nominal overlap number of pulses. All data were also recorded on magnetic tape for a later detailed analysis.

In Fig. I-13(a), (b), (c), and (d), the measured E(x), in the focal plane, has been plotted for a single pulse after steady state for N_o = 1.46, 2.41, 4.88, and 9.41. The solid-line distribution is that predicted by the code using the Gaussian aperture distribution and measured experimental parameters (α, E_p, R, D_x, ν). Differences between theory and experiment are typically smaller than the experimental uncertainty in a simple measurement.

To address a comprehensive comparison of experiment with theory, measurements were made of the energy redistribution over a range of absorption coefficients corresponding to cell transmittances of 83 to 47 percent, pulse energies of 6 to 7 joules, and overlap conditions of N_o = 2.35, 4.75, and 9.5 pulses per aperture-clearing-time. Complete bloomed and unbloomed focal distributions were measured for each pulse. To characterize the blooming with a single number, the peak energy on a single 1 × 15-mm array element was chosen. To reduce experimental scatter resulting from variations in pulse energy and/or beam quality, the peak focal energy measured in the bloomed pulse was normalized to the peak measured in the unbloomed beam. (For experimental details see Fig. I-4, Optics Research Report 1974:2.) Overall system response was determined from empty cell conditions. To define blooming for a given condition, typically three pulses in each train were measured after steady state and averaged. At least two experiments under the same conditions were always performed. Using this procedure successive measurements differed by less than five percent.

During the data reduction process, a source of beam motion was identified that modified the nominal overlap number during the measurement period. Rotating burn pattern drums recorded the focal distributions from the input beam sampled at the laser and the output beam that was measured after traversing all external optical elements. Under empty cell (α = 0) conditions, both burn pattern records yield the same beam position information. Consequently, any beam motion must originate at the laser. In Fig. I-14, the deviation of the beam from its mean lateral position has been plotted as a function of pulse number and times for a nominal overlap condition of 9.5. In this instance, the steady-state distribution would be characterized by the average of pulses 11, 12, and 13. It can be seen that during the measurement there is a small net velocity contribution (~3 cm/sec) to the otherwise constant-velocity crosswind. The net effect of the perturbation can be treated as a modification to the overlap number, i.e., $N_e = N_o + \delta N_o$ where N_e is the effective overlap number. Taking the variation on N_o (= $D_x/v\tau$),

$$\delta N_o = \frac{D_x}{(v\tau)^2}\,\delta(v\tau) = \frac{\delta(v\tau)}{D_x}\,N_o^2 \quad .$$

The convergence of blooming to steady state is sufficiently rapid to accommodate small velocity changes on a pulse-to-pulse basis making a perturbation approximation reasonable. It can be seen that the effect of beam jitter is very significant at high overlap numbers but that the perturbation expressed as a fraction of the total aperture width is a scaled effect that will probably not

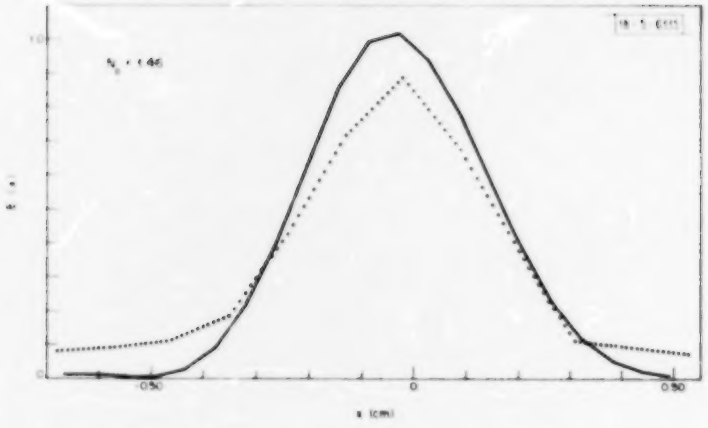

(a)

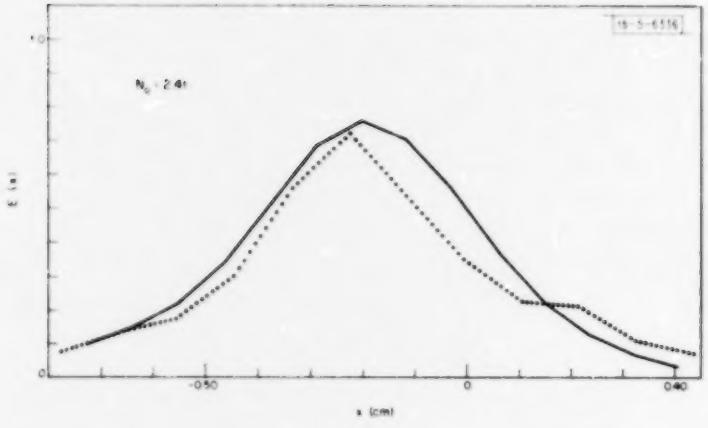

(b)

Fig. I-13. One-dimensional focal distributions for bloomed beams for overlap numbers, N_D = (a) 1.46, (b) 2.41, (c) 4.88, (d) 9.42. Dotted lines are measurements; solid lines are theoretical predictions using Gaussian approximation.

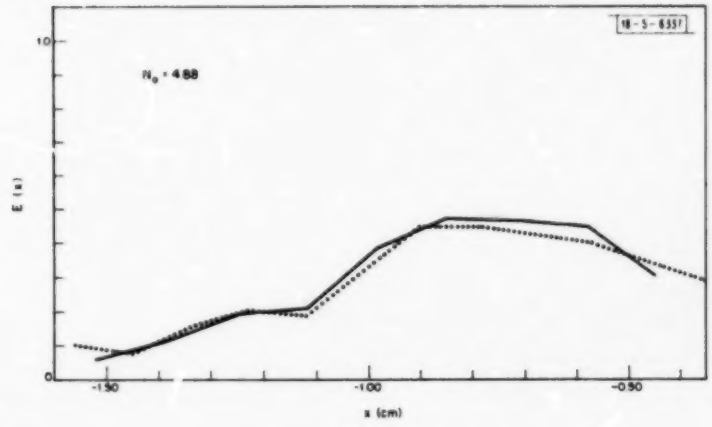

(c)

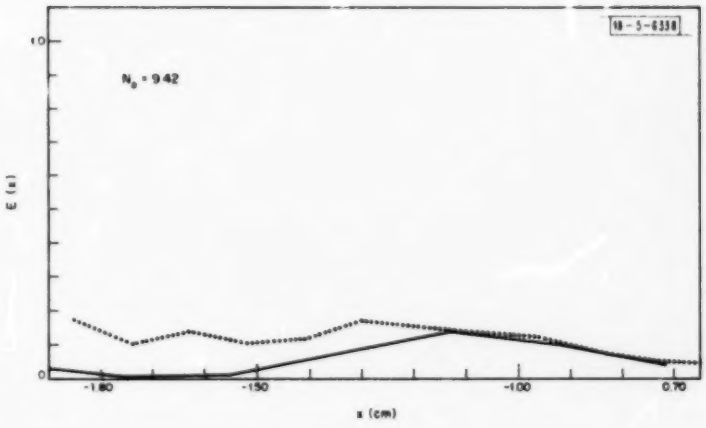

(d)

Fig. I-13. Continued.

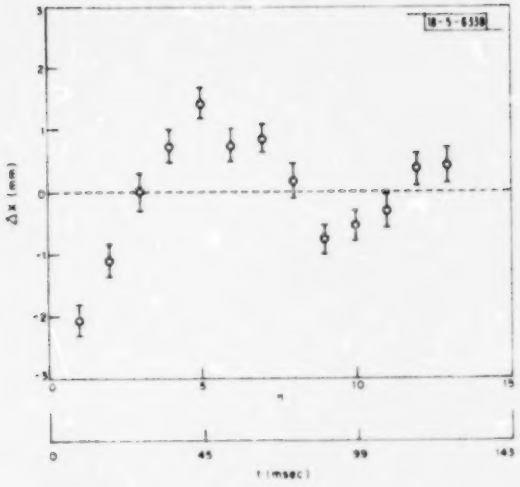

Fig. I-14. Beam motion superimposed on constant crosswind for N_O = 9.46 as function of pulse number and time. Solid lines are ±3 percent and dashed lines are ±1 percent variation in $(v\tau)/D_x$.

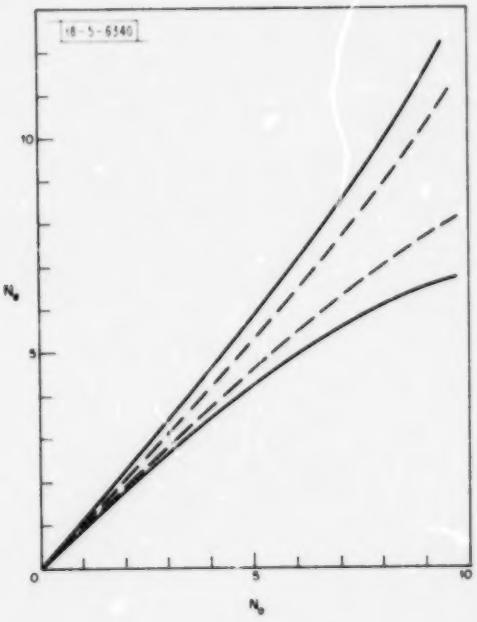

Fig. I-15. Plot of the effective overlap number, N_e, due to ordered laser beam jitter plotted as a function of nominal overlap number, N_O.

be significant in large beams. Figure I-15 is a plot of N_e vs N_o for $\delta(v\tau)/D_x = \pm 1$ and ± 3 percent, the range of the observed variation projected to the entrance to the absorption cell.

If we take this beam jitter effect into account in presenting data, the theoretical predictions appear as bands indicative of a range in overlap numbers appropriate to the superposition of the disturbance motion on the otherwise constant-velocity wind. In Fig. I-16, the peak energy normalized to empty cell conditions has been plotted as a function of $\alpha E_p R/D_x^2$. Experimental points are plotted with maximum absolute error bars. There are no adjustable parameters.

In Fig. I-17, the shift of the peak energy into the wind caused by thermal blooming has been plotted as a function of N_c for $\alpha E_p R/D_x^2 = 1.1$. The shaded region illustrates the theoretical predictions. Beyond $N_o = 5$ the focal distribution breaks up too severely to define an energy peak. For other experimental conditions, the agreement between theory and experiment is typical of that illustrated in Fig. I-17.

From the data presented above, it can be seen that on a laboratory scale, the Bradley and Herrmann steady-state model for multiple-pulse blooming predicts accurately the absolute reduction in far-field energy density and the shift in focal position. Reasonable agreement is found using an approximate aperture distribution but a more detailed amplitude and phase description should improve the accuracy of the calculation. Laser beam jitter found to be a primary limit in this small-scale comparison should not be a serious problem in larger scale experiments.

R. W. O'Neil
H. R. Zwicker
D. H. Dickey
L. C. Pettingill
A. P. Ferdinand

3. Fog Blooming Measurements

Initial experimental results have been obtained of second-pulse blooming of a high-energy CO_2 laser pulse propagating through a laboratory fog environment. The primary purpose of the experiment was to bore a hole through a fog with the first pulse[5] and then to measure the second-pulse blooming induced by the expanding index spheres resulting from the vaporization of the fog droplets.

The Lincoln Laboratory dual 500-J CO_2 pulsed-laser facility was used for the measurements. A schematic of the experimental setup is shown in Fig. I-18. The two laser pulses are brought into a collinear geometry with the use of a germanium beam splitter and then focussed downrange with a 30-m focal length mirror. Transmission gratings, G1 and G2, were used to generate side orders for beam diagnostics. Photon drag detectors, $BaTiO_3$ calorimeters, and pyroelectric detector arrays placed in the focal plane were used to monitor the pulse shape, total energy, and spatially resolved energy distribution of the individual laser pulses. The artificial fog was generated in a 5-m-long chamber placed in the propagation path as shown in Fig. I-18. The fog density (water content) and equivalent particle size were determined using techniques described in Ref. 5.

The second-pulse blooming was measured as a function of pulse separation, Δt_p, which ranged from 1 to 42 msec and for a range of fog densities from 2 to 8 gm/m^3. These fog densities were chosen to scale to the total water content of light to moderate atmospheric fogs over a propagation path length of 1 km.

The results of a preliminary analysis of the data are summarized in Fig. I-19 in which a measure of the blooming is taken as the ratio of the half-widths (full widths at half maximum) of the transmitted and incident spot sizes as measured in the focal plane. Figure I-19(a) shows

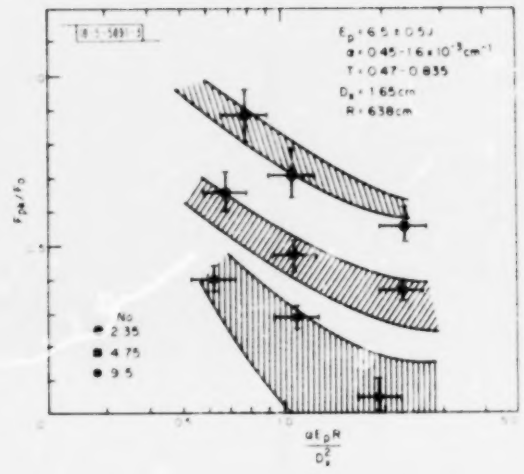

Fig. I-16. Normalized peak energy measured on a detector array element plotted as a function of $\alpha E_p R/D_x^2$ for N_o = 2.35, 4, 5, and 9.5.

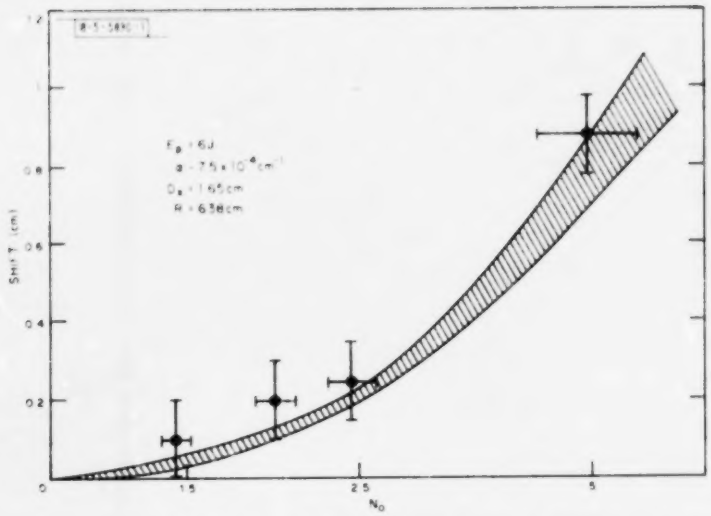

Fig. I-17. Blooming-induced shift in focal position plotted as a function of N_o for $\alpha E_p R/D_x^2$ = 1.1.

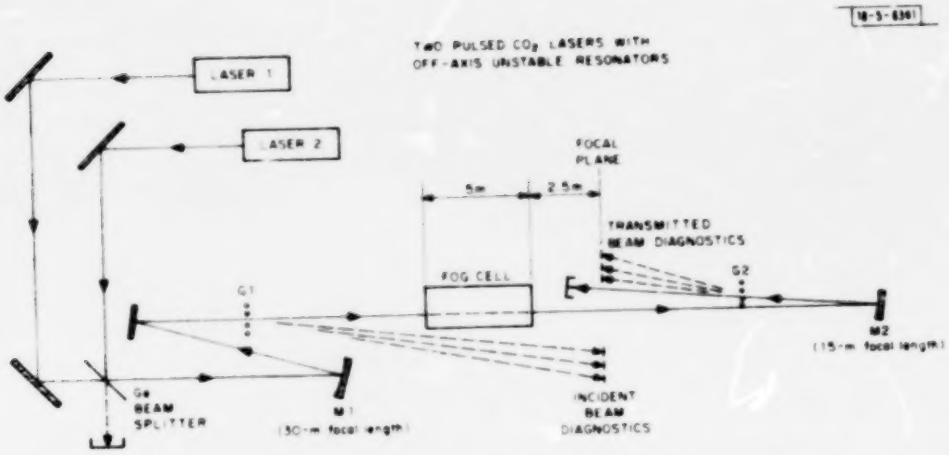

Fig. I-18. Experimental setup for fog blooming experiment.

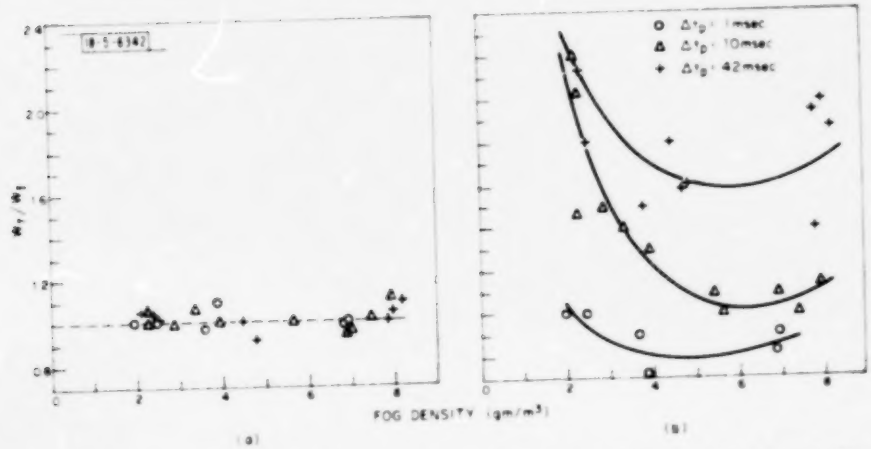

Fig. I-19. Measure of blooming defined as the ratio of transmitted to incident half-widths of the spot size measured in the focal plane as a function of fog density (a) for first pulse and (b) for second pulse.

the ratio of the half-widths of the clearing (first) pulse as a function of fog density. The ratios tend to cluster about a value of one indicating that there is negligible first-pulse blooming. The spread of the data of ±10 percent provides an indication of the measurement accuracy. The second-pulse blooming is shown in Fig. I-19(b). Two trends are apparent. First, the blooming generally increases with increasing pulse separation, Δt_p. Second, for a fixed Δt_p, the blooming tends to decrease with increasing fog density and appears to approach a minimum at a fog density of 6 to 8 gm/m^3. Although, at present, there is no integrated theory with which to compare these results, the latter trend is contrary to expectation. In a zeroth-order approximation, one would expect the second-pulse blooming to increase monotonically with increasing fog density. The preliminary analysis indicates that the "bored hole," i.e., the volume in which the fog droplets have been completely vaporized by the first pulse, is smaller than the geometrical volume of both the first and second laser pulses as measured without the presence of fog. The possibility that this incomplete clearing may be at least partially responsible for the decrease of measured blooming with increasing fog density and, in addition, the apparent focussing of the second pulse for the Δt_p = 1 msec case is currently being investigated. The analysis and interpretation of the data is continuing.

S. K. Manlief
A. P. Ferdinand

B. LASER EFFECTS

1. Large-Spot Thermal Coupling Measurements

Recent thermal coupling measurements[6-8] at this and other laboratories have shown that if the incident laser intensity is sufficient to cause a breakdown at a target surface, the coupling coefficient can differ markedly from its low-intensity value. Specifically, for normally highly reflecting metals, such as aluminum, enhancement of an order of magnitude or more has been observed. This enhancement is due to the high absorptivity of the generated plasma and subsequent efficient transfer of energy to the target surface.

Those measurements, however, were done with relatively small spot size, and as we have previously shown,[7] for such small spots a significant fraction of the energy is transferred by the expanding plasma to the target outside of the local spot and is therefore of little benefit in reducing the burn-through time.

As the laser spot size is increased, the fraction of energy deposited by the expanding plasma that remains within the focal area is expected to increase, and definite fluence coupling enhancement should be observed. We report here experimental results which confirm this expectation.

The experiments were performed with one of our 500-J CO_2 lasers, which was fitted with a germanium outcoupled stable resonator. With this choice of cavity, a very nearly uniform beam was generated and directed with a 2-m focal length mirror onto a thermocoupled target. The spot size at the target was adjusted by moving the focusing mirror along the optical axis. In this manner, effects with spot areas up to 19 cm^2 were observed. A beam splitter, photon drag detector and $BaTiO_3$ calorimeter were used to monitor the pulse shape and energy on each shot, while plasma plumes were observed with a photomultiplier and open-shutter photography.

Figure I-20 shows a plot of thermal coupling coefficient (α) vs incident laser fluence (E/A) for three different-sized rear-thermocoupled aluminum targets. (In this and subsequent figures, the lines through the points are merely for convenience in viewing and do not represent a fit to a theoretical curve.) The absorbed energy was determined by measuring the bulk temperature

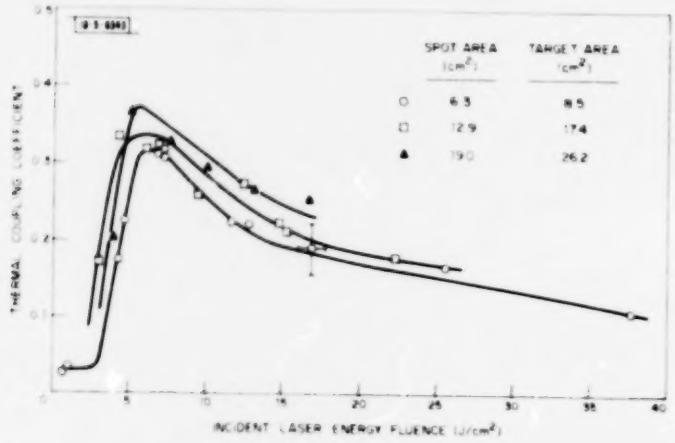

Fig. I-20. Spot size dependence of thermal coupling to an aluminum target, the typical error is shown for one point.

increase of the target. Spot areas of 6.3, 12.9 and 19.0 cm^2 were used, which in each case were approximately 12 percent smaller in linear dimension than the target. The coupling coefficients obtained therefore are a measure of energy deposited near the focal spot. It is seen from these curves that above breakdown threshold, there is a considerable enhancement in coupling over the low-intensity value, which peaks near threshold and decreases with increasing laser fluence. Moreover as the spot size is increased, the degree of enhancement in coupling coefficient is also increased somewhat. This indicates that for larger spots, a slightly larger fraction of the incident energy is coupled to the target in the focal spot area.

As is shown in Fig. I-21, the coupling coefficients we have measured peak at comparable values to those measured by Rudder[6] at AFWL with his small (0.062 cm^2) focal spot, but fall off much faster with increasing laser fluence. This results in part from the fact that for equal

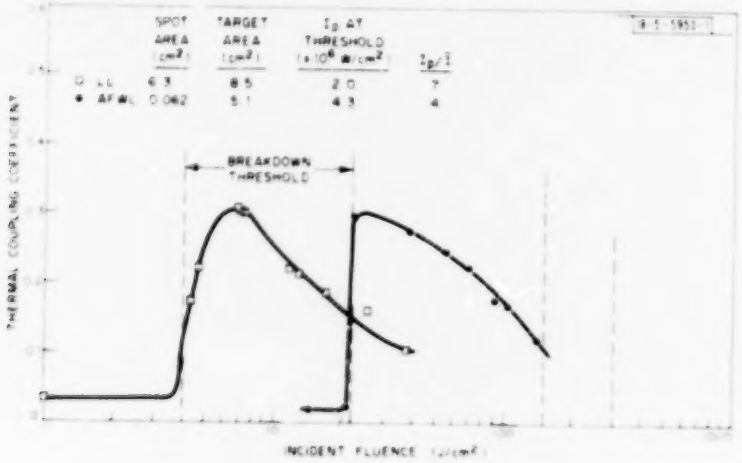

Fig. I-21. Pulsed thermal coupling to aluminum at 10.6 μm.

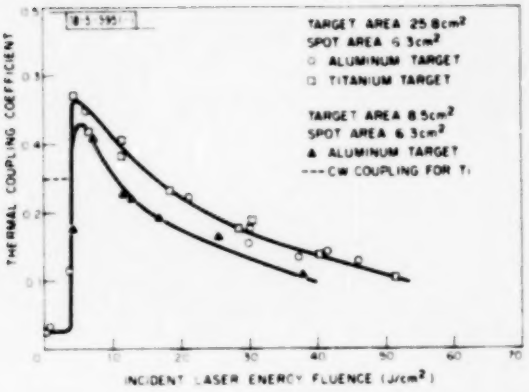

Fig. I-22. Material and target-size dependence of thermal coupling.

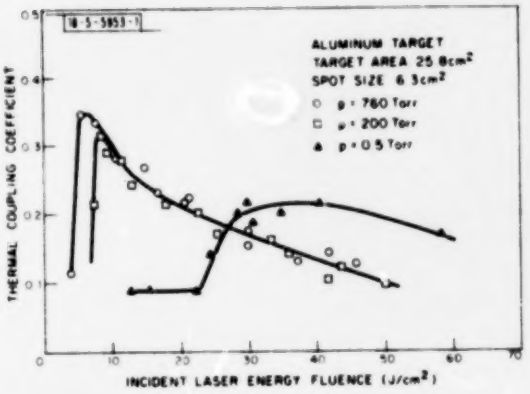

Fig. I-23. Pressure dependence of thermal coupling.

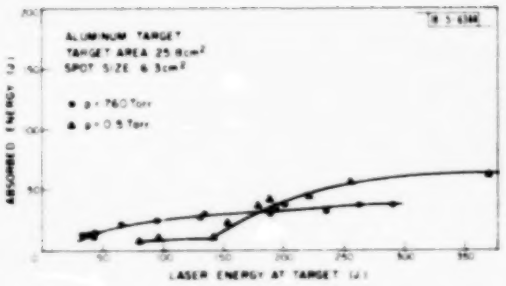

Fig. I-24. Pressure dependence of absorbed energy.

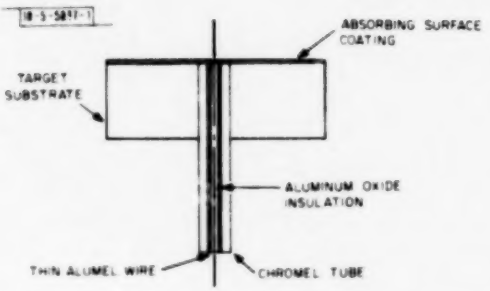

Fig. I-25. Surface-thermocoupled target structure.

laser intensities, more plasma energy is dissipated radially for a very small spot than for a larger one, thus reducing the plasma density and hence the velocity at which it recedes from the surface. Therefore, at high intensities and small focal spots, the laser energy is absorbed closer to the target and is more efficiently transferred to it. It should be kept in mind, however, that for such small spots most of the energy is absorbed by the target outside the focal spot.

Another contributor to the rapid fall-off of the thermal coupling coefficient with E/A in our case may be the large and relatively broad initial spike associated with our cavity design (see Fig. I-26). Klosterman et al.[9] have observed and Jackson and Nielsen[10] have calculated that the shock associated with ignition of an absorption wave can raise its propagation velocity substantially over what it would be were the wave translating into quiescent air. This increased velocity was found to persist long after ignition. If that be the case, our strong spike, which in all cases induces the breakdown, may increase considerably the velocity at which the absorption wave recedes from the target, even after the spike is over. This would result in a more effective decoupling of the laser radiation than would be the case were there no spike.

To test the above hypothesis, we propose to perform thermal coupling experiments with the spike eliminated or greatly reduced. We have previously demonstrated that this can be done, using either saturable absorbers or electron-gun current modulation. Streak photography will be employed to determine the effect of the spike on the propagation velocity of the plasma.

Figure I-22 shows a plot of thermal coupling coefficient vs E/A for two 2 in. × 2 in. (25.8 cm^2) targets – one aluminum and one titanium. In both cases the spot area was 6.3 cm^2. Also shown is the plot from Fig. I-20 in which the spot area was also 6.3 cm^2, but the target area was only 8.5 cm^2. We see that the above breakdown threshold, the curves for aluminum and titanium are identical to within the scatter of the data, indicating that in this regime, the absorptivity is controlled by the plasma and is independent of target material. If the target is normally highly absorbing, this may in fact result in a decrease in coupling coefficient, as is the case for titanium at high incident fluence. By comparing the two curves for aluminum, we see as well that a relatively small fraction of the energy is absorbed far from the focal spot.

Coupling data were also obtained for aluminum targets as a function of ambient air pressure, and the results are plotted in Fig. I-23. The measured values of α at 200 Torr are quite close to those at 760 Torr except for the difference in breakdown threshold. The curve changes markedly, however, as the pressure is reduced to 0.5 Torr. Although the coupling is less than in air at low fluences, it surpasses it at about 26 J/cm^2 and peaks (at a lower value than at 760 Torr) at about 40 J/cm^2. This behavior is due to diffuseness of the air plasma at this low pressure. These results imply that, as shown in Fig. I-24, considerably more energy per unit area can be deposited on a target at high altitude than at sea level.

In order to determine the spatial distribution of the absorbed energy, we fabricated several targets of the surface-thermocoupled type previously used to obtain our small spot data. In this type of target, as shown in Fig. I-25, coaxial thermocouples are inserted flush with the surface, and a thin coating of the metallic absorber to be investigated is then deposited over it. The targets used in this study contained a linear array of six aluminum-coated thermocouples, 1/4 in. apart, enabling us to determine the absorbed energy distribution both inside and outside the focal spot.

Figure I-26 shows a comparison of the pulse shapes of the incident and absorbed intensity for a point inside the focal spot. The pulses are normalized to equal areas. It is seen that the initial spike is quite efficient in coupling energy to the surface since the plasma has not moved

Fig. I-26. Pulse shapes of incident and absorbed intensity.

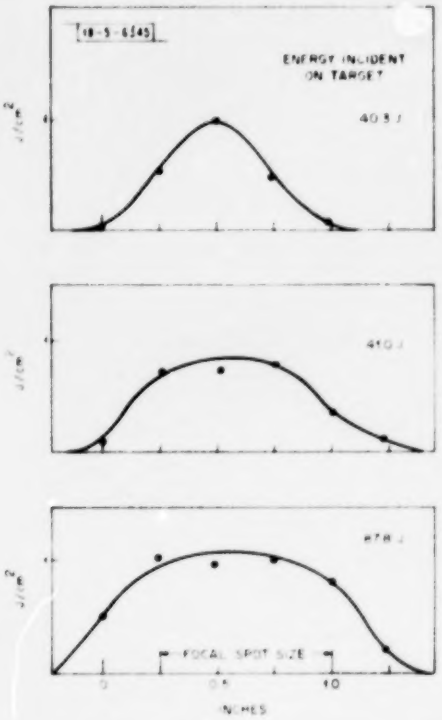

Fig. I-27. Spatial distribution of absorbed energy for three different incident laser energies.

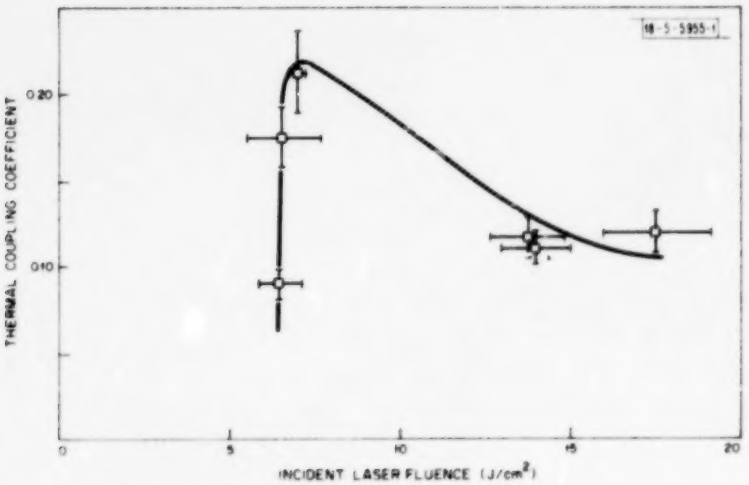

Fig. I-28. Pulsed thermal coupling coefficient as deduced from front surface temperature measurements.

appreciably. As the plasma recedes, decoupling sets in. At the end of the pulse, however, an appreciable amount of energy is still being absorbed. This indicates that increasing the pulse length may increase the maximum deliverable fluence.

Figure I-27 shows the absorbed fluence in air as a function of position for three different incident laser energies, the top two being very near breakdown threshold. These fluences were extracted from the observed temperature histories by means of a computer inversion of the one-dimensional heat equation. These curves clearly show the spreading of the absorbed energy distribution as the laser energy is increased.

The absorbed fluence distribution can then be integrated spatially to give the total energy absorbed by the target and the thermal coupling coefficient as a function of incident laser fluence. Figure I-28 shows such a coupling coefficient curve. This curve is similar to those of Fig. I-20 except that the breakdown threshold occurs at higher fluences, and the peak absorptivity is somewhat lower. This is most likely due to the smoother surface of the deposited aluminum.

We may summarize this work by the following conclusions.

(a) Enhancement of thermal coupling is retained with large focal spots, but the coupling decreases faster with incident laser fluence than with small spots.

(b) The fraction of energy coupled to the target within the focal spot increased with increasing spot size.

(c) Above the target-dependent breakdown threshold, the thermal coupling is material independent.

(d) For high incident fluences, more energy is transmitted to the target at 0.5 than at 760 Torr.

(e) Experiments should be done to determine the effect on thermal coupling of
   (1) Removing or reducing the initial spike and
   (2) Increasing the pulse length.

S. Marcus R. L. Mooney
J. E. Lowder (Aeronutronic Ford)

2. Microwave Measurements of a Laser-Generated Surface Plasma

Preliminary measurements have been made on microwave transmission, reflection, and in-band radiation for a laser-generated surface plasma.

The experimental arrangement is shown in Fig. I-29. A 20-MW X-band source operated at 9.5 GHz was used to transmit the test signal to a receiving antenna located ≈3 m from the transmitter horn. A 1/8-in. Lucite sheet placed over the transmitting horn acted as the target for the high-energy laser pulse. E- and H-plane tuners were used to null the reflected signal from the target in the absence of a surface plasma. The reflected signal from a surface plasma passed through a 10-dB directional coupler and low-pass filter ($f < 10$ GHz). The amplitude of the transmitted and reflected signals was measured with crystal detectors T and R. The detectors when used with 2-kohm terminations had a time constant ≈1 μsec. A reference level for the reflected signal (total reflection) was obtained by placing a copper sheet on the target surface.

The target surface was located 7.5 m in front of the laser beam focus at which point the beam size was ≈4 × 3 cm. Pulses with energies ≈120 J in ≈10 μsec and with a 5-to-1 spike

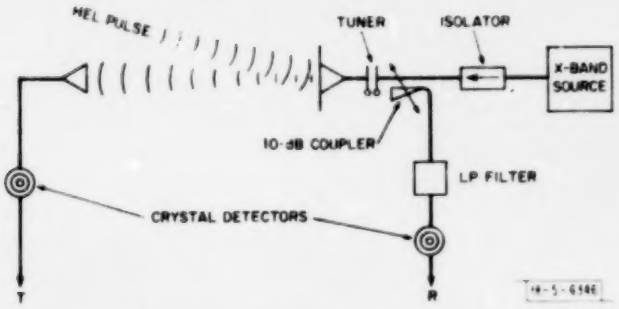

Fig. I-29. Experimental arrangement for microwave transmission and reflection measurements.

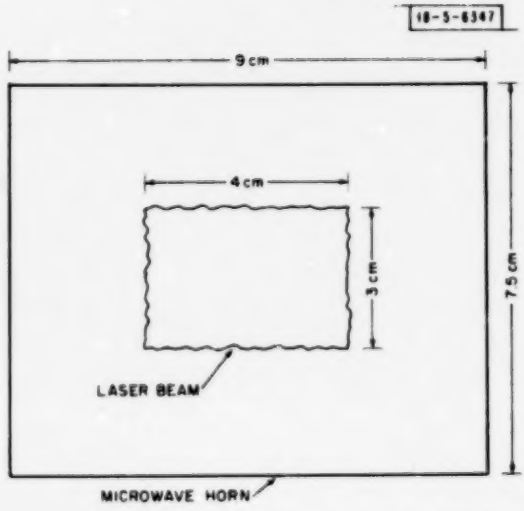

Fig. I-30. Relative size of laser beam to transmitting horn.

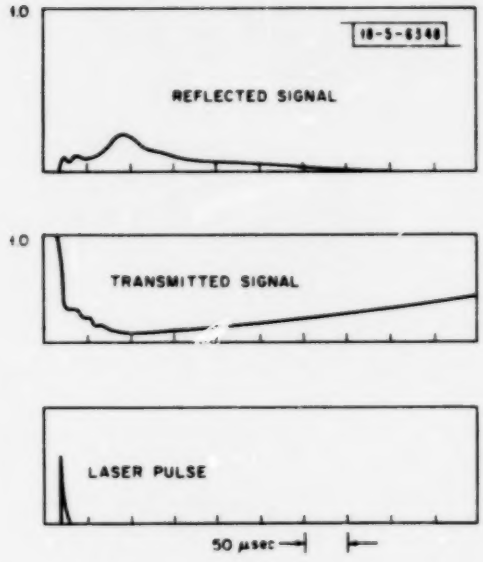

Fig. I-31. Reflected and transmitted microwave signals as a function of time after laser pulse.

were used to generate the surface plasma. The peak intensities were $\approx 5 \times 10^6$ W/cm^2. The relation between the beam size and transmitting-horn dimensions is shown in Fig. I-30. Note that the initial plasma fills only a small fraction of the transmitter aperture.

Figure I-31 shows the results for the transmitted and reflected microwave signals as a function of time after the laser pulse. The transmitted signal drops to a minimum value and the reflected signal rises to a maximum value at $\approx$70 μsec after the laser pulse. This is probably due to the fact that the initial plasma size is smaller than the transmitting horn. If 70 μsec is taken as the time required for the plasma to expand and fill the horn, the corresponding radial velocity would be $\approx 3.4 \times 10^4$ cm/sec. It is expected that if the transmitting antenna were smaller than the initial plasma size then the reflected signal would be a maximum and the transmitted signal would be a minimum just after the laser pulse. Note from Fig. I-31 that the transmitted signal has recovered to only 50 percent of the maximum value after 0.5 msec, indicating the presence of a low-level electron density for long times.

An attempt to detect microwave emission from the plasma was made with the X-band source turned off. The geometry was the same as in Fig. I-29 but with antenna T placed $\approx$10 cm from the surface plasma. No detectable microwave plasma radiation was observed.

The above results are consistent with theoretical estimates of the plasma behavior. First consider the reflection and transmission properties. These are determined by the parameters:[11]

ω = microwave frequency

ω_p = plasma frequency $\propto \eta_e^{1/2}$

ν = electron collision frequency = $f(T_e)$

d = plasma thickness

Initially the plasma density and temperature are both large and $\omega_p \gtrsim \nu > \omega$. So that[1]

$$R \approx 1$$
$$T \approx 0 \quad ;$$

that is, the plasma acts like a totally reflecting conductor.

At the later times the density and temperature decay so that $\nu \gtrsim \omega > \omega_p$. In this limit the plasma acts as a lossy dielectric with

$$R = 0$$

and an absorption depth

$$\delta = \frac{2c(\omega^2 + \nu^2)}{\omega_p^2 \nu} \quad .$$

For the microwave radiation an estimate can be made in terms of a blackbody at temperature T for λ = 3 cm and $\Delta\lambda$ = 1 cm. This gives $dP/dA = 3.2 \times 10^{-14}$ T W/cm^2. Even for 10^4 K and A = 10^2 cm^2

$$P \sim 3 \times 10^{-8} \text{ watts}$$

which is well below the detectable with the present apparatus.

These initial experiments indicate that anomalously large microwave plasma radiation was not present, and that the reflection and transmission of microwaves was consistent with theory.

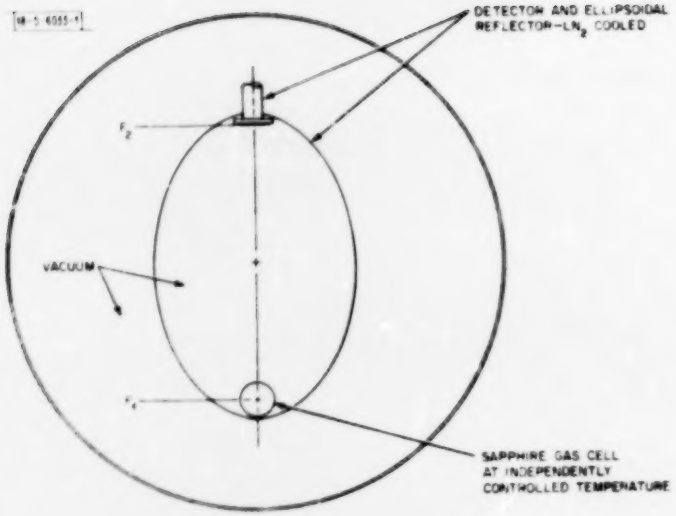

Fig. I-32. Schematic illustration of the new external CO_2 reference gas cell.

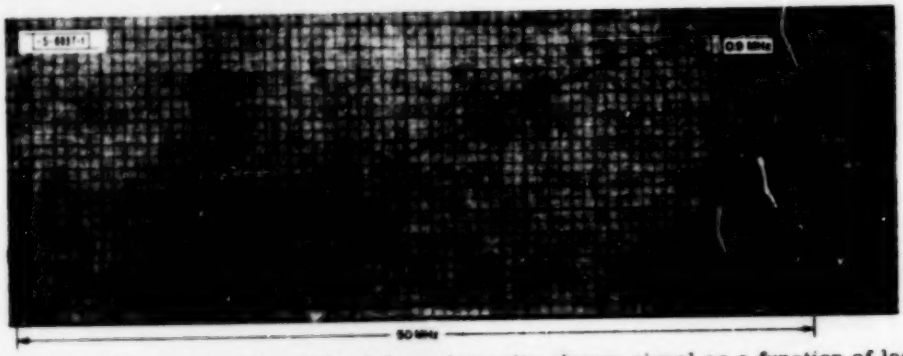

Fig. I-33. Recorder tracing of the 4.3-μm intensity change signal as a function of laser frequency tuning in the P(20) transition at 10.59 μm. Modulation frequency: 260 Hz, power input to the cell: 1.75 W, cell pressure: 0.034 Torr.

The experimental technique described above can in principle be used to obtain quantitative information on the electron density and temperature in the decaying surface plasma for times $\gtrsim 50$ μsec.

D. E. Lencioni

C. LONG-TERM FREQUENCY STABILIZATION OF CO_2 LASERS

This report will illustrate some of the new results obtained with the improved CO_2 long-term stabilization setup by means of the 4.3-μm $(00^01) \rightarrow (00^00)$ fluorescence technique.[12,13,14] In the last Optics Research Report, it was briefly mentioned that we have designed, tested, and built new, low-pressure CO_2 stabilization cells external to the lasers. In the new cells, significantly larger signal collection efficiency is achieved simultaneously with a great reduction in background radiation, which is the primary limit in high-quality InSb photovoltaic detectors.

In the new design, the low-pressure gas cell, the LN_2-cooled radiation collector, and the IR detector are all integral parts of one evacuated housing assembly which minimizes signal absorption by windows and eliminates all other sources of absorption. Because of the vacuum enclosure, diffusion of other gases into the low-pressure gas reference cell is almost completely eliminated; therefore, the time period available to use the reference gas cell has greatly increased and considerably less time has to be wasted on repumping and refilling procedures. Also, one LN_2 fill will last at least 18 hours. Figure I-32 schematically illustrates the new external reference gas cell used in the 4.3-μm stabilization setup. In addition to greatly improved reliability and maintenance, we have also obtained at least two orders of magnitude improvement of the signal-to-noise ratio in measuring the 4.3-μm fluorescence.

Figure I-33 shows a typical recorder tracing of the observed 4.3-μm intensity change as the laser frequency is tuned across the 10.59-μm P(20) line profile with 0.034 Torr pressure of CO_2 absorber gas. The standing-wave saturation resonance appears in the form of a narrow resonant 16.4-percent "dip" in the 4.3-μm signal intensity as the laser frequency is tuned across the center frequency of the absorbing transition's Doppler profile. The broad background curve is due to the laser power variation as the frequency is swept within its oscillation bandwidth. Since collision broadening in the CO_2 absorber is about 7.6 MHz/Torr FWHM,[12] in the limit of very low gas cell pressures the linewidth is determined by power broadening and by the molecular transit time across the diameter of the incident beam. The potentially great improvements in signal-to-noise ratio, in power and transit time broadening, and in short-term laser stability were the primary motivating factors that led to the choice of stabilizing cells external to the laser's optical cavity.

The one disadvantage inherent with the use of external stabilizing cells is that appropriate precautions must be taken to avoid optical feedback into the lasers to be stabilized.

For frequency reference and long-term stabilization, it is convenient to obtain the derivative of the 4.3-μm emission signal as a function of frequency. This 4.3-μm signal derivative may be readily obtained by modulating the laser frequency by a small amount as we slowly tune across the resonance in the vicinity of the absorption-line center frequency. With the use of standard phase-sensitive detection techniques, we can then obtain the 4.3-μm derivative signal to be used as a frequency discriminator. Figure I-34 shows such a 4.3-μm derivative signal as a function of laser tuning near the center frequency of the 10.59-μm P(20) transition

Figure I-34 also illustrates the signal- and noise-level amplitudes we have chosen to derive the signal-to-noise ratios of the frequency discriminants in this paper. More than half of the

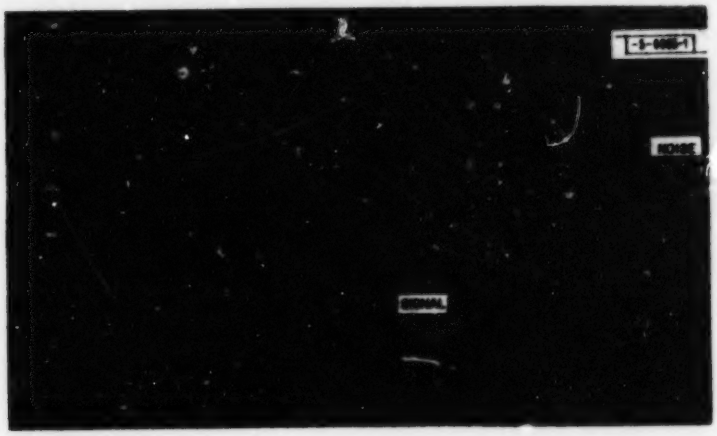

Fig. I-34. Recorder tracing of the 4.3-μm derivative signal as a function of laser frequency tuning near the center frequency of the P(20) transition at 10.59 μm; the frequency dither is set to ±5 kHz at a 260-Hz rate. Power input to the cell: 1.75 W, cell pressure: 0.034 Torr.

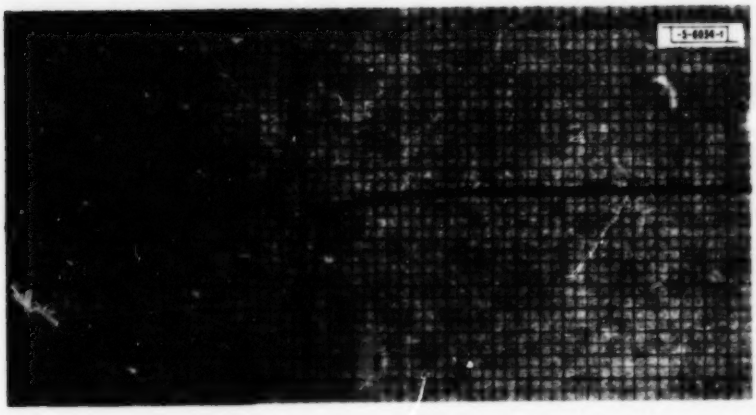

Fig. I-35. Recorder tracing of the 4.3-μm derivative signal as a function of laser frequency tuning near the center frequency of the P(20) transition at 10.59 μm; the frequency dither is set to ±20 kHz at a 260-Hz rate. Power input to the cell: 1.75 W, cell pressure: 0.034 Torr.

noise was caused by background photon current noise $\overline{i_p^2} = 2eI_p\Delta f$, with the remainder primarily due to residual 1/f noise. As Fig. I-34 shows, the noise levels were chosen near the peak-to-peak rather than the rms value. A single RC filter with a 0.1-sec risetime was used to measure all the 4.3-μm signal and noise results shown in this paper. Thus, the S/N data presented here were obtained with a noise bandwidth which was 20 times wider than the one we have used in previously published experiments.[12,14] Obviously, we could have shown much larger S/N values by using longer noise averaging times; nevertheless, the wide-bandwidth data were considered more appropriate for usability in closed-loop stabilization schemes.

Figure I-35 shows another 4.3-μm derivative signal with a ±20-kHz frequency dither which we used to lock one laser to the center of the P(20) absorption profile. Figure I-36 shows the spectrum analyzer display of the beat note of two lasers. One of the lasers was line-center locked by using the discriminant shown in Fig. I-35, while the other laser was free running with a frequency offset of about 8 MHz. If both lasers were synchronously modulated at a 260-Hz rate with a ±20-kHz peak deviation of the 10.59-μm P(20) laser output, the beat note appeared as a relatively narrow single spectral line and is shown in the left half of Fig. I-36. The right half of Fig. I-36 illustrates a typical FM signal spectrum which resulted when the modulation signal was disconnected from the free-running laser.

Figure I-36 also demonstrates at least qualitatively the effectiveness of our recently designed feedback electronics. The laser remained firmly locked to the line center with as little as ±2 kHz frequency dither. Respective rise times of 0.001 and 0.03 sec were used in the phase-sensitive detector and in the high-voltage integrating amplifier of the servo loop.

Figure I-37 illustrates the signal, noise, and S/N obtained with ±100 kHz dithering of the laser. Figure I-38 provides a summary of the signal-to-noise ratios as a function of peak frequency deviation at a 260-Hz rate. The results summarized in Fig. I-38 were obtained with a $^{12}C^{16}O_2$ 10.59-μm P(20) laser power of about 1.75 watts. The absorption cell diameter, the beam diameter (at the 1/e field) and beam divergence were about 22.2 mm, 11.8 mm, and 1.5×10^{-3} radian, respectively. The CO_2 ce l pressure was purposefully chosen to be about 0.034 Torr to provide easy comparison with previously published results.[12,14,15,16]

The relatively slow decay[17,18] of the spontaneous 4.3-μm radiation arising from the $(00^01) \rightarrow (00^00)$ transition seriously limits the maximum frequency that can be effectively used to modulate the CO_2 lasers. Figure I-39 clearly illustrates the loss of the 4.3-μm signal with increasing modulation frequency. The 4.3-μm decay rate is primarily determined by cell pressure and geometry. Consideration of detector 1/f noise may well dictate an optimum modulating frequency which is higher than would be indicated by considering the signal alone. As an example, Fig. I-40 shows the signal, noise, and S/N as a function of modulation frequency for one of our reference cells. From Fig. I-40 it is clear that at 0.034 Torr pressure the optimum modulating frequency is approximately 500 Hz, in spite of some loss of signal at this frequency.

In conclusion, we have designed, tested and built new, low-pressure CO_2 stabilization cells external to the lasers in which significantly larger signal collection efficiency was achieved simultaneously with a great reduction in background radiation, which was the primary limit in high-quality InSb photovoltaic detectors.

We have evaluated and tested several large-area InSb detectors and determined that cooled background greatly diminishes 1/f noise in addition to the expected reduction in the white noise due to the lower temperature background radiation.

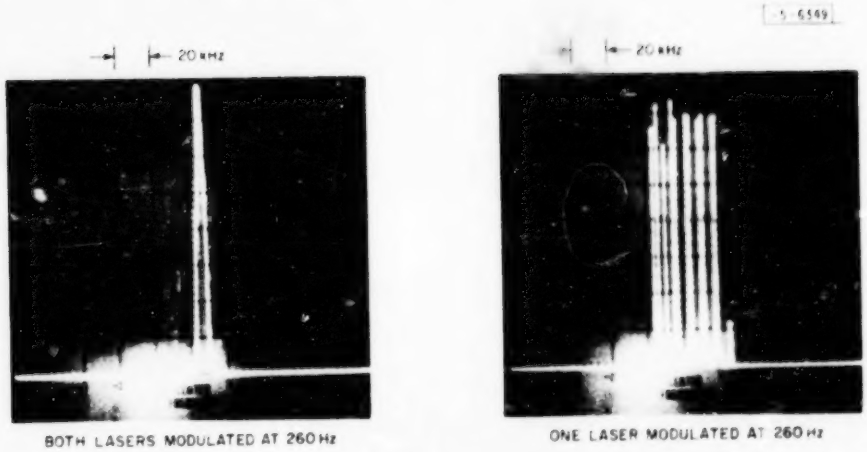

Fig. I-36. Spectrum analyzer display of the beat note of two lasers with one laser locked to the line center and the other offset by 8 MHz and free running.

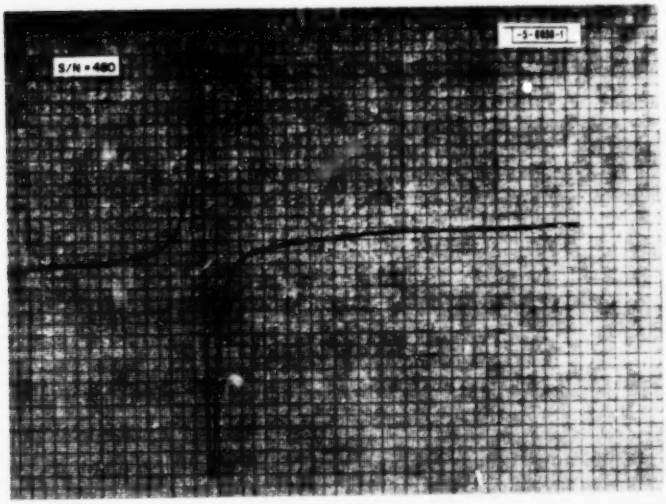

Fig. I-37. Recorder tracing of the 4.3-μm derivative signal as a function of laser frequency tuning near the center frequency of the P(20) transition at 10.59 μm; the frequency dither is set to ±100 kHz at a 260-Hz rate. Power input to the cell: 1.75 W, cell pressure: 0.034 Torr.

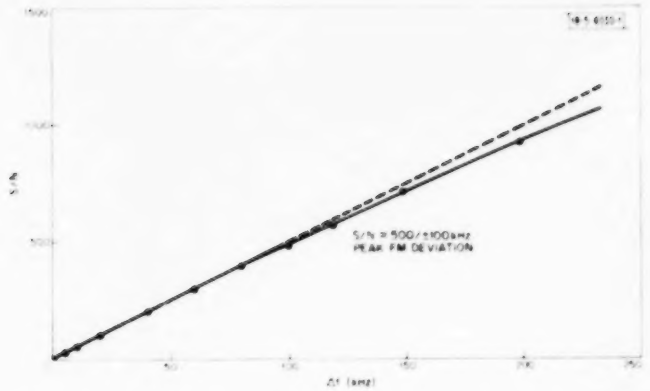

Fig. I-38. Signal-to-noise ratio as a function of peak frequency dither at a 260-Hz rate. Power input to the cell: 1.75 W, cell pressure: 0.034 Torr, FWHM ~0.9 MHz.

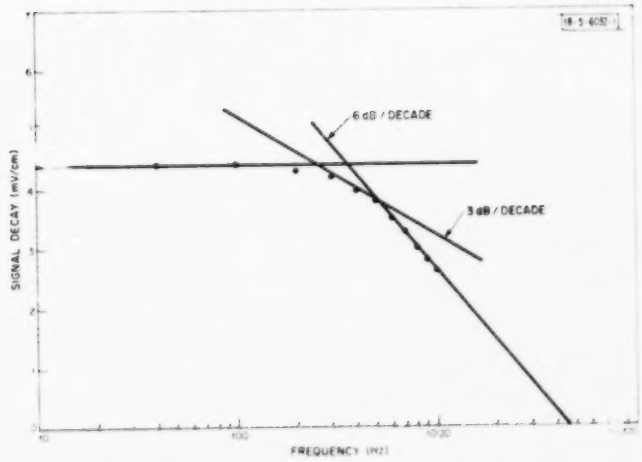

Fig. I-39. 4.3-μm signal decay as a function of modulation frequency. Cell pressure: 0.05 Torr, cell diameter: 22.2 mm.

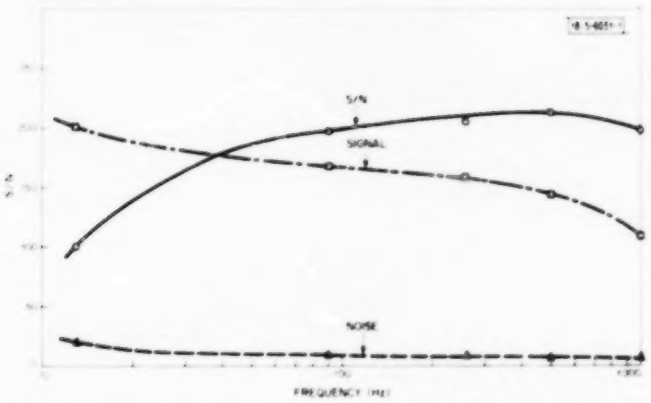

Fig. I-40. Signal, noise, and signal-to-noise ratio as a function of modulation frequency for a 22.2-mm-diameter cell filled with 0.034 Torr CO_2 at +14 °C temperature. Frequency dither is set to ±40 kHz. Power input to the cell: 1.75 W, laser transition: $00^01 - [10^00, 02^00]_I$ P(20), FWHM ~0.9 MHz; 16.4 percent dip.

Significant improvements in signal-to-noise ratios have been achieved with the new stabilization cells, together with greatly improved reliability and maintenance.

By utilizing frequency-stabilized CO_2 isotope lasers and optical heterodyne techniques, the band centers, rotational constants, and operating frequencies of the various CO_2 isotopes are being determined with great accuracy.

C. Freed

REFERENCES

1. L. C. Bradley and J. Herrmann, Appl. Optics 13, 331 (1974).
2. Optics Research Report, Lincoln Laboratory, M.I.T. (1973:1), DDC AD-770629.
3. Optics Research Report, Lincoln Laboratory, M.I.T. (1973:2), DDC AD-779917/4.
4. Optics Research Report, Lincoln Laboratory, M.I.T. (1974:2), DDC AD-A10476.
5. J. E. Lowder, H. Kleinman, and R. W. O'Neil, J. Appl. Phys. 45, 221 (1974).
6. R. R. Rudder, First DoD Conference on High Energy Laser Technology, San Diego, California, 1-3 October 1974.
7. S. Marcus, J. E. Lowder, S. Manlief, and D. L. Mooney, Conference on Laser Engineering and Applications, Washington, D.C., 28-30 May 1975; Optics Research Report, Lincoln Laboratory, M.I.T. (1974:2), DDC AD-A10476.
8. R. B. Hall, J. D. McClure, W. E. Maher, D. B. Nichols, and P. S. P. Wei, Interim Progress Report, Contract Number F29601-73-A-0038-6002, Boeing Aerospace Company (February 1975).
9. F. L. Klosterman, S. R. Byron, J. F. Newton, "Laser Supported Combustion Waves Study," Interim Report, Air Force Weapons Laboratory (1973).
10. J. P. Jackson and P. E. Nielsen, AFWL Laser Digest, AFWL-TR-74-100, 212 (1974).
11. M. A. Heald and C. B. Wharton, "Plasma Diagnostics with Microwaves," Wiley (1965).
12. C. Freed and A. Javan, "Standing-Wave Saturation Resonances in the 10.6 μm Transitions Observed in a Low-Pressure Room-Temperature Absorber Gas," Appl. Phys. Lett. 17, 53-56 (1970).
13. C. Freed and A. Javan, "Standing-Wave Saturation Resonances in Room Temperature CO_2 10.6 μm Absorption Lines," Paper 4.4 presented at the 1970 Sixth International Quantum Electronics Conference, September 1970, Kyoto, Japan.
14. C. Freed, "Designs and Experiments Relating to Stable Lasers," Proceedings of the Frequency Standards and Metrology Seminar, University Laval, Quebec, Canada, 226-261, 1 September 1971.
15. F. R. Petersen, D. G. McDonald, J. D. Cupp, and B. L. Danielson, "Accurate Rotational Constants, Frequencies, and Wavelengths from $^{12}C^{16}O_2$ Lasers Stabilized by Saturated Absorption," Proceedings of the Laser Spectroscopy Conference, Vail, Colorado, 25-29 June 1973.
16. T. W. Meyer, "Line Broadening and Collisional Studies of CO_2 Using the Techniques of Saturation Spectroscopy," Ph.D. Thesis, University of California, Lawrence Livermore Laboratory, UCRL-51561, April 1974.
17. M. Kovacs, D. Ramachandra Rao, and A. Javan, "Study of Diffusion and Wall De-excitation Probability of 00^01 State in CO_2," J. Chem. Phys. 48, No. 7, 3339-3341 (1968).
18. L. Doyennette, M. Margottin-Maclou, H. Gueguen, A. Carion, and L. Henry, "Temperature Dependence of the Diffusion and Accomodation Coefficients in Nitrous Oxide and Carbon Dioxide Excited into the (00^01) Vibrational Level," J. Chem. Phys. 60, No. 2, 697-702 (1974).

II. POLLUTION STUDIES*

A. PARTICIPATION IN THE ST. LOUIS REGIONAL AIR POLLUTION STUDY (RAPS) OF THE U.S. ENVIRONMENTAL PROTECTION AGENCY

1. Introduction

The technique of resonance absorption in the infrared has been used to perform integrated-path monitoring of ambient carbon monoxide (CO) in the St. Louis area recently, as part of the Regional Air Pollution Study. Measurements made last spring (1974) in Massachusetts demonstrated that over a path 0.6 km long the detection sensitivity for CO was a few parts per billion (ppb), with no interference problems. The laser system was then incorporated into a mobile van and transported to St. Louis where measurements were made at three different sites over the two-month period from mid-August to mid-October 1974.

Details of tunable diode laser pollution measurement techniques over long ambient paths have been described elsewhere in Refs. 1-3.

2. RAPS Measurements – Summary

During the first period of measurements in St. Louis from mid-August to mid-October 1974, the following was accomplished:

(a) Comparative tests were made of pollutant variability using the long-path laser technique in conjunction with bag samples and off-line gas chromatographic analysis. These tests support our measurement and calibration techniques, but also showed that, as expected, there can be wide variations in CO concentration depending on location of the sampler.

(b) Long-path ambient CO data were obtained at three different sites (St. Louis University, RAMS site 108, and RAMS site 105) to be used as input data for the various mathematical models under consideration.

(c) Near the end of our stay in St. Louis, a direct on-line comparison was made between the laser monitor and a sensitive, real-time point-sampler instrument developed under another EPA program.

(d) Transfer of the laser technology to EPA personnel was initiated.

3. RAPS Measurements – Data

The relative locations of the three field sites we used are shown in Fig. II-1. Site 106.5 is located on the St. Louis University campus, and was chosen for the short-path comparison tests with point-sampling instruments such as the bag sampler and portable monitor. The second site, 108, is located on a farm in Illinois north of Granite City. It should be a variable-pollution site, depending on wind speed and direction. The third site, 105, is located in downtown St. Louis, and represents an inner-city site where automobile traffic is an important factor in the CO pollution level.

---

*This section describes the work performed at Lincoln Laboratory under the sponsorship of the National Science Foundation (Research Applied to National Needs), with partial support from the U.S. Environmental Protection Agency.

PRECEDING PAGE BLANK-NOT FILMED

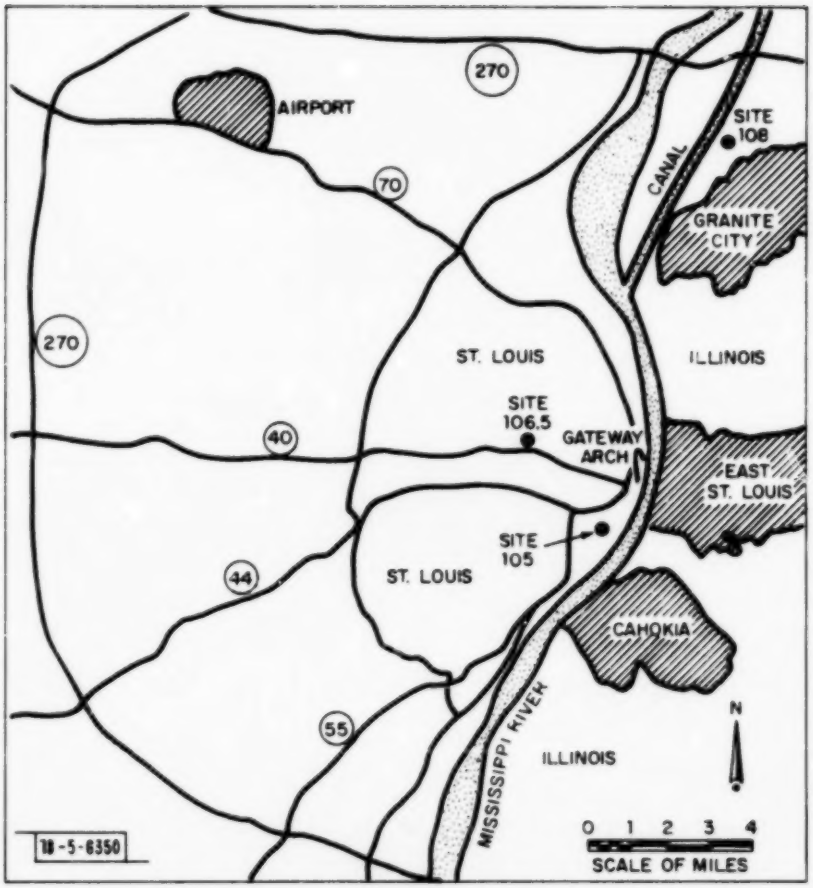

Fig. II-1. Field site locations for laser monitoring in the St. Louis area.

a. Data at Site 106.5 (St. Louis University)

For these experiments, the van was parked next to a football field, permitting bag samples to be taken along the entire path which extended to 0.3 km.

For the comparative study, bag samples were taken while walking along the path of the laser beam. Figure II-2 is a typical comparison, where the continuous curve is the laser monitor result of the CO level averaged over the path during the period in which the bag was filled. The average value from the laser measurement was 0.6 ppm, which compares favorably with the bag result of 0.56 ppm (parts per million).

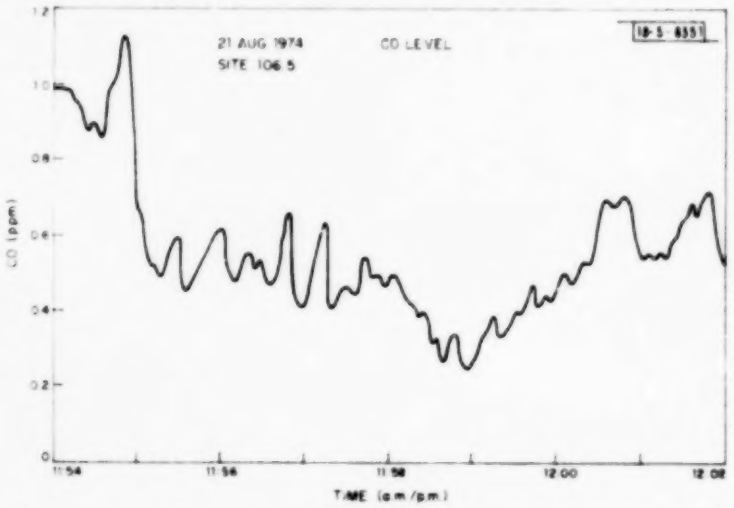

Fig. II-2. Laser long-path measurement of CO over 8-min. period at Site 106.5 (St. Louis University). The time-averaged laser reading is 0.60 ppm. For comparison, bag samples taken over the same period along the same path, and analyzed later by conventional gas chromatography, yielded a value of 0.56 ppm. Path length = 0.34 km, integration time = 1 sec for laser measurement.

Table I summarizes the comparisons made at this site. We notice generally good agreement between the results; of course, the accuracy of such a comparison is determined in large part by the spatial and temporal variations in pollutant concentration over the monitoring path.

b. Data at Site 108 (Farm in Illinois)

The laser monitoring van was parked next to the RAMS (Regional Air Monitor) station off Pontoon Road. The predominant feature of this site is the soy bean field. Our retroreflector was placed at various points along a levee to change the path length and perform path variability studies. The longest distance over which monitoring was performed here was 1 km (between laser and retroreflector). Figure II-3 shows a typical trace of CO concentration at this site, averaged over 10-min. intervals (the original data were taken within a 1-sec time constant). The circles represent the CO readings from a gas-chromatographic (Beckman 4800) instrument inside the RAMS station. Even though the path length was much longer than that at Site 106.5, good correlation was obtained between the laser and point-monitor results. This indicates to

TABLE I

COMPARATIVE CO MEASUREMENTS AT SITE 106.5
(St. Louis University)

Date	Laser (ppm)	Bag Samples (ppm)
August 20	0.55	0.61
August 21	0.60	0.62
August 21	0.39	0.56
August 22	1.65	1.07
August 26	0.87	1.02
August 29	3.10	2.30
August 30	2.13	1.93
August 30	0.95	0.82
September 3	0.76	0.74
		0.64
		0.68
		0.68

On 3 September, four bag samples were taken simultaneously from points at equal intervals along the 200-m path.

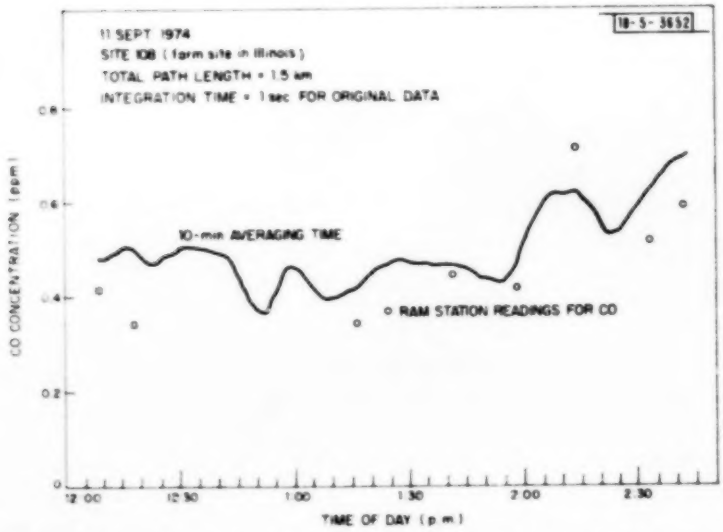

Fig. II-4. Long-path diode laser monitoring results for CO at Site 108 (solid curve), and Regional Air Monitoring Station readings (circles).

us that the pollution concentration was fairly uniform over the area at this remote farm site, due, perhaps, to the absence of local pollution sources such as heavy automobile traffic.

c. Data at Site 105 (Inner-City)

The van was parked next to a RAMS station in the downtown St. Louis area.

We were able to direct the laser beam to either the top of the Monsanto building, 0.6 km away, or to the top of the Anheuser-Busch building, 1 km away. Redirecting the beam from one target to the other takes approximately one minute.

Figure II-4 shows the integrated-path concentration of CO to the Anheuser-Busch building. As expected for this inner-city site, the pollutant level is higher than for either of the other two sites, and the level fluctuated over a much wider range. In order to illustrate the spatial variation in CO concentration over the laser beam path, bag samples were taken at 1:35 p.m. and

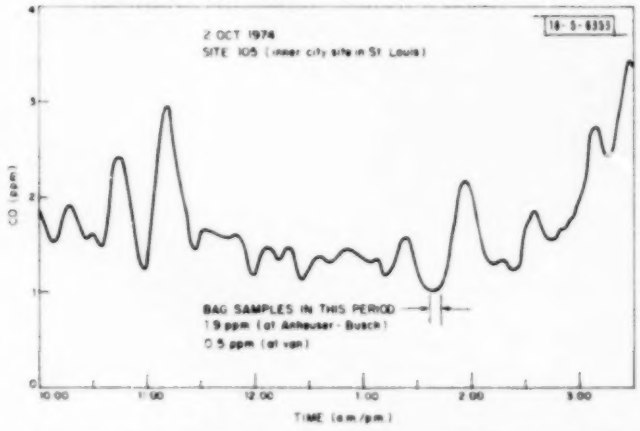
2 OCT 1974
SITE 105 (inner city site in St Louis)
BAG SAMPLES IN THIS PERIOD
1.9 ppm (at Anheuser-Busch)
0.5 ppm (at van)
CO (ppm)
TIME (a.m./p.m.)

Fig. II-4. Long-path measurements of CO at Site 105 over 5 1/2-hour period. Comparative bag samples taken between 1:35 and 1:45 p.m. (see Fig. II-5). Path length = 2 km, integration time = 10 min.

1:45 p.m. at the van and Anheuser-Busch building, respectively. These values are compared with the result in the expanded time scale of Fig. II-5. The laser-obtained average over the path was 1.1 ppm, whereas that obtained by sampling at Anheuser-Busch was 1.9 ppm, and from a sample at the van, 0.5 ppm (nearly four times smaller). We might suspect even wider variations closer to the highway traffic.

4. Future Plans

Most of the mathematical pollution models have grid structures of the order of 1 km, and the type of long-path data shown here should be useful both for providing input data on pollution levels and checking model predictions. We plan to extend the monitoring capability of the diode laser system to other gases, namely NO, O_3, and NH_3 during the coming year. In addition, it may be possible to increase the path length (to 5 or 10 km) to obtain greater sensitivity for weakly absorbing gases such as SO_2 and provide wider spatial coverage for the regional models.

R. T. Ku
E. D. Hinkley
J. O. Sample

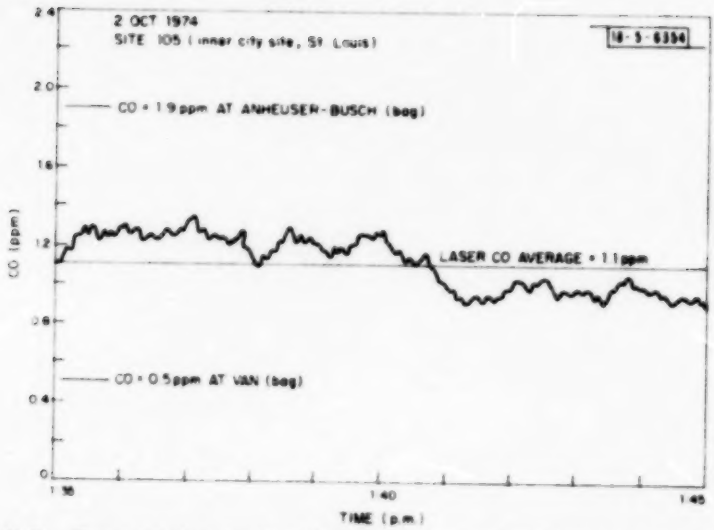

Fig. II-5. Comparative study of long-path laser monitoring results (solid curve) and bag samples taken at both ends of the path (values indicated by horizontal lines near ordinate). Path length = 2 km, integration time = 1 sec.

Fig. II-6. Photograph of monitored path across Kendall Square, Cambridge, with retroreflector (on tripod) in foreground.

B. LONG-PATH AMBIENT MONITORING OF NITRIC OXIDE

Ambient levels of nitric oxide (NO) were monitored at Kendall Square in Cambridge, Massachusetts, over a path length of 440 m with our pollution monitoring van. The detection and measurement techniques are essentially similar to those of carbon monoxide (CO) described in Refs. 1-3. However, an appropriate $PbS_{1-x}Se_x$ laser chemically tailored to operate at 5.3 μm was used to match resonant absorption lines of NO around 1930 cm^{-1}, where H_2O vapor does not interfere significantly.

In Fig. II-6, we have a photograph taken at Kendall Square looking from the retroreflector toward the van. The laser path traversed a traffic rotary, 11 to 12 ft above ground level. Typical NO monitoring results are shown in Fig. II-7. The data were recorded with a 1-sec time constant. Large, abrupt increases in the NO level can be attributed to the exhausts from diesel-fueled trucks and buses. The sharp decay of the NO level after its initial increase is probably due to the fact that NO reacts strongly with O_3 in the air and converts rapidly to nitrogen dioxide (NO_2). In order to observe the general trend of NO concentration during the day, NO was monitored with a 10-sec averaging time, such as shown in Fig. II-8. The ambient level rose to above

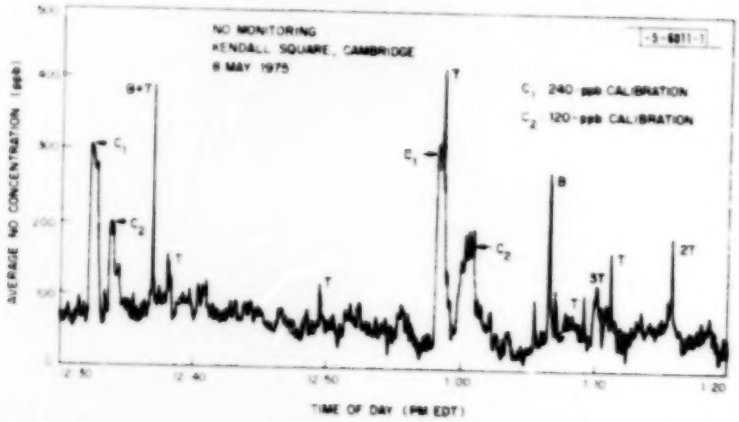

Fig. II-7. Continuous long-path monitoring of nitric oxide (NO) at Kendall Square. The letters "T" and "B" indicate the passage of trucks and buses, respectively (apparently diesel-powered because of the large NO emissions). System calibrations were performed at times indicated by "C." Path length = 440 m, time constant = 1 sec.

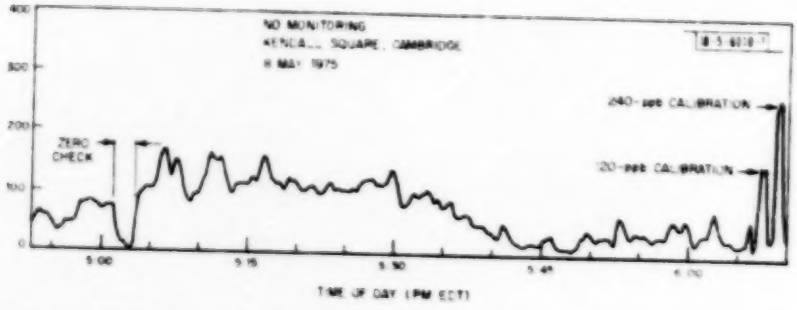

Fig. II-8. Rush-hour monitoring of nitric oxide at Kendall Square. Path length = 440 m, time constant = 10 sec.

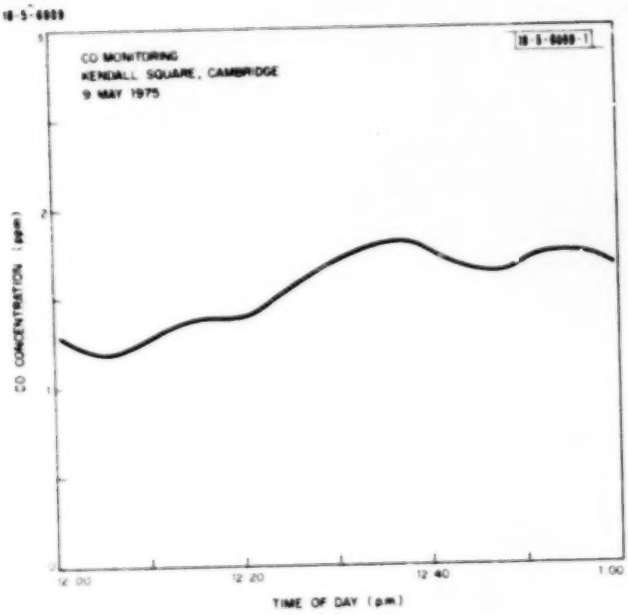

Fig. II-9. Continuous monitoring of carbon monixide at Kendall Square using diode laser operating at 4.7 μm. Path length = 440 m, time constant = 5 min.

100 ppb (parts per billion) around 5 p.m. due to traffic, and leveled off to less than 50 ppb after 5:30 p.m.

The CO concentration over the path can also be monitored by switching to a second diode laser operating at 4.7 μm, mounted next to the NO laser in the cryogenic cooler. The change-over generally takes only a few minutes. Figure II-9 shows the CO-monitored results with a 5-min. time constant around 12:30 p.m. over the same ambient path.

E. D. Hinkley
R. T. Ku
J. O. Sample

REFERENCES

1. R. T. Ku, E. D. Hinkley, and J. O. Sample, Appl. Optics 14 854, (1975).
2. Optics Research Report, Lincoln Laboratory, M.I.T. (1974:1), p. 37, DDC AD-A001971.
3. Optics Research Report, Lincoln Laboratory, M.I.T. (1974:2), p. 37, DDC AD-A10476.

UNCLASSIFIED

SECURITY CLASSIFICATION OF THIS PAGE (When Data Entered)

REPORT DOCUMENTATION PAGE	READ INSTRUCTIONS BEFORE COMPLETING FORM
1. REPORT NUMBER: ESD-TR-75-252	2. GOVT ACCESSION NO. / 3. RECIPIENT'S CATALOG NUMBER
4. TITLE (and Subtitle): Optics Research; 1995:1.	5. TYPE OF REPORT & PERIOD COVERED: Semiannual Report, 1 Jan - 30 June 1975. / 6. PERFORMING ORG. REPORT NUMBER: Optics Research (1975:1)
7. AUTHOR(s): Rediker, Robert H.	8. CONTRACT OR GRANT NUMBER(s): F19628-73-C-0002
9. PERFORMING ORGANIZATION NAME AND ADDRESS: Lincoln Laboratory, M.I.T. P.O. Box 73 Lexington, MA 02173	10. PROGRAM ELEMENT, PROJECT, TASK: ARPA Order 600
11. CONTROLLING OFFICE NAME AND ADDRESS: Advanced Research Projects Agency 1400 Wilson Boulevard Arlington, VA 22209	12. REPORT DATE: 30 June 1975 / 13. NUMBER OF PAGES: 56
14. MONITORING AGENCY NAME & ADDRESS (if different from Controlling Office): Electronic Systems Division Hanscom AFB Bedford, MA 01731	15. SECURITY CLASS. (of this report): Unclassified / 15a. DECLASSIFICATION DOWNGRADING SCHEDULE

16. DISTRIBUTION STATEMENT (of this Report)

Approved for public release; distribution unlimited.

17. DISTRIBUTION STATEMENT (of the abstract entered in Block 20, if different from Report)

18. SUPPLEMENTARY NOTES

None

19. KEY WORDS (Continue on reverse side if necessary and identify by block number)

optics
laser technology
thermal blooming
optical devices
optical systems
adaptive mirror
thermal coupling

20. ABSTRACT (Continue on reverse side if necessary and identify by block number)

This report covers work of the Optics Division at Lincoln Laboratory ~~for the period 1 January through 30 June 1975~~. The topics covered are laser technology and propagation and pollution studies.

Additional information on the optics program may be found in the ARPA/STO Program Semiannual Technical Summary Reports to the Advanced Research Projects Agency.

DD FORM 1 JAN 73 1473 EDITION OF 1 NOV 65 IS OBSOLETE

UNCLASSIFIED

SECURITY CLASSIFICATION OF THIS PAGE (When Data Entered)

207 650